

A Nested Grid Model of the Oregon Coastal Transition Zone: Simulations and Comparisons with Observations During the 2001 Upwelling Season

S. R. Springer¹, R.M. Samelson¹, J. S. Allen¹, G. D. Egbert¹, A. L. Kurapov¹, R. N. Miller¹

and J. C. Kindle²

¹College of Oceanic and Atmospheric Sciences, Oregon State University, Corvallis, Oregon, USA.

²Oceanography Division, Naval Research Laboratory, Stennis Space Center, Mississippi, USA.

Submitted to *Journal of Geophysical Research*

04/10/2008

AGU Index terms: 4217 Oceanography: General: Coastal processes
4219 Oceanography: General: Continental shelf processes (3002)
4255 Oceanography: General: Numerical modeling (0545, 0560)
4263 Oceanography: General: Ocean predictability and prediction (3238)

Corresponding author address:

Scott R. Springer
COAS Admin. Bldg 104A
College of Oceanic and Atmospheric Sciences
Oregon State University
Corvallis, OR 97331
Email: springer@coas.oregonstate.edu

Report Documentation Page			<i>Form Approved OMB No. 0704-0188</i>	
<p>Public reporting burden for the collection of information is estimated to average 1 hour per response, including the time for reviewing instructions, searching existing data sources, gathering and maintaining the data needed, and completing and reviewing the collection of information. Send comments regarding this burden estimate or any other aspect of this collection of information, including suggestions for reducing this burden, to Washington Headquarters Services, Directorate for Information Operations and Reports, 1215 Jefferson Davis Highway, Suite 1204, Arlington VA 22202-4302. Respondents should be aware that notwithstanding any other provision of law, no person shall be subject to a penalty for failing to comply with a collection of information if it does not display a currently valid OMB control number.</p>				
1. REPORT DATE 10 APR 2008	2. REPORT TYPE	3. DATES COVERED 00-00-2008 to 00-00-2008		
4. TITLE AND SUBTITLE A Nested Grid Model of the Oregon Coastal Transition Zone: Simulations and Comparisons with Observations During the 2001 Upwelling Season			5a. CONTRACT NUMBER	
			5b. GRANT NUMBER	
			5c. PROGRAM ELEMENT NUMBER	
6. AUTHOR(S)			5d. PROJECT NUMBER	
			5e. TASK NUMBER	
			5f. WORK UNIT NUMBER	
7. PERFORMING ORGANIZATION NAME(S) AND ADDRESS(ES) Oregon State University, College of Oceanic and Atmospheric Sciences, Corvallis, OR, 97331			8. PERFORMING ORGANIZATION REPORT NUMBER	
9. SPONSORING/MONITORING AGENCY NAME(S) AND ADDRESS(ES)			10. SPONSOR/MONITOR'S ACRONYM(S)	
			11. SPONSOR/MONITOR'S REPORT NUMBER(S)	
12. DISTRIBUTION/AVAILABILITY STATEMENT Approved for public release; distribution unlimited				
13. SUPPLEMENTARY NOTES Submitted to Journal of Geophysical Research				
14. ABSTRACT see report				
15. SUBJECT TERMS				
16. SECURITY CLASSIFICATION OF: b. ABSTRACT unclassified			17. LIMITATION OF ABSTRACT Same as Report (SAR)	18. NUMBER OF PAGES 59
a. REPORT unclassified	c. THIS PAGE unclassified			

Abstract

The Oregon Coastal Transition Zone (OCTZ) extends several hundred kilometers offshore where shelf flows interact with the northern California Current. A primitive-equation numerical ocean model is used to study the upwelling circulation in this region from May 1 to November 1, 2001. This OCTZ model obtains initial and boundary conditions from a larger-scale model of the California Current System and forcing from a regional atmospheric model product. The model results are compared with extensive in situ and remotely sensed data, and the model is found to provide a useful representation of flows both over the shelf and in the broader OCTZ. Simulation of coastal sea level and shelf currents over the complex topography of the central Oregon coast is improved quantitatively relative to previous regional models. A particularly significant qualitative improvement is realistic representation of coastal jet separation and eddy formation offshore of Cape Blanco. A three-dimensional Lagrangian analysis of water parcel displacement shows that the surface waters inshore of the separated jet are upwelled from near the bottom along the shelf as far north as 45.5° N. A large eddy, which incorporates some of this upwelled water and carries it farther westward, forms offshore in the late summer. Ensemble simulations point toward a distinction between the strongly deterministic response to wind forcing over the shelf, and more unstable, less predictable jet separation and offshore eddy formation processes in the region near Cape Blanco.

1. Introduction

Near the eastern boundary of the north Pacific Ocean, the southward flow of the California Current is influenced by coastal circulation. Beginning in early spring and lasting until late fall, southward winds force coastal upwelling, which contributes to the formation of a narrow, surface-intensified southward jet [Huyer, 1983]. Water properties differ on either side of the jet, with relatively colder, saltier, more nutrient rich, and more biologically productive waters on the shoreward side. During the summer and early fall the jet separates from the coastline near Cape Blanco (42.8° N), a major headland on the Oregon coast [Barth *et al.*, 2000]. South of that location the separated current forms jets, plumes, and eddies in an area that extends hundreds of kilometers offshore [Strub and James, 2000]. This area over which mesoscale and sub-mesoscale features mix the distinctive shelf and slope waters with those of the open ocean is known as the coastal transition zone [Brink and Cowles, 1991]. Here we focus on the Oregon Coastal Transition Zone (OCTZ), which extends from the north side of Cape Mendocino, California, (40.5° N) to north of Cape Elizabeth, Washington, (47.3° N) and approximately 400 km offshore.

The complexity of flow in the OCTZ indicates that a numerical modeling approach will be valuable in understanding the dynamical processes involved and the pathways taken by water parcels from shelf to open ocean. Because of disparate time and space scales of the shelf and open ocean, past modeling studies have tended to focus on one or the other, neglecting interaction between the two. Modeling studies of the central Oregon shelf [Oke *et al.*, 2002 a,b; Kurapov *et al.*, 2005 a, b, c; Gan and Allen, 2005a; Gan *et al.* 2005] have used high horizontal (1-2 km) and vertical resolution (up to 60 sigma levels) to represent topographic influences and boundary layer structure. Forced by winds with daily temporal resolution, such models realistically simulate flows on the inner and mid-shelf for periods of 50-100 days, but none develop separation of the coastal jet at Cape Blanco, mesoscale eddies, or

realistic flow in the offshore region because of deficiencies in the boundary condition formulation. On the other hand, these features of the large-scale circulation have been simulated in models of the California Current System (CCS; e.g. *Batteen* [1997], *Shulman* [2004]), but the horizontal (typically 9–10 km) and vertical grid resolutions and temporal resolution of the forcing are inadequate to simulate details of the circulation on the narrow Oregon shelf. In the cases where the entire CCS is modeled at sufficiently high spatial resolution [*Marchesiello et al.*, 2003; *Powell et al.*, 2006], little attention has been paid to comparing the shelf circulation with observations.

In this study, a one-way, nested grid model is developed to study the interaction of shelf flows with the CCS in the OCTZ. The spatial resolution is sufficient to represent the shelf circulation and the effects of the large-scale circulation are imposed through boundary conditions. The finite difference model, nesting method, and forcing are described in section 2. Model-simulated circulation during the upwelling season of 2001 is described in Section 3 and is compared with a wide variety of observational data, with particular attention paid to the central Oregon shelf, to evaluate the realism of the simulated circulation. In Section 4, some aspects of the shelf circulation are interpreted in terms of coastal trapped wave theory, Lagrangian pathways from the shelf offshore into the deep ocean are explored, and a small ensemble of model runs with slightly different initial conditions is analyzed to evaluate the relative importance of disturbance growth and deterministic response. Conclusions are presented in Section 5.

2. Model and data

2.1 Model Description

The OCTZ model is based on the Regional Ocean Modeling System (ROMS version 2.2; *Shchepetkin and McWilliams* [2005]; *Haidvogel et al.* [2007]), a discretization of the hydrostatic

primitive equations with a free surface. A parabolic splines density Jacobian scheme is used for pressure gradient calculations [*Shchepetkin and McWilliams*, 2003], and a third-order, upwind-biased scheme is used in horizontal momentum and tracer advection. A fourth-order, centered scheme is used for vertical advection of tracers. Sub-gridscale mixing is parameterized by the Mellor-Yamada Level 2.5 model in the vertical direction [*Mellor and Yamada*, 1982; *Wijesekera et al.*, 2003], and by harmonic diffusivity and viscosity, both with coefficients of $20 \text{ m}^2/\text{s}$, in the horizontal direction. Lateral diffusion of tracers is restricted to isopycnals to minimize problems related to the interaction of strong horizontal mixing and steep bottom topography [*Dinniman and Klinck*, 2002].

The domain extends from 40.6° N to 47.5° N and from 123.7° W to 129° W , approximately 400 km offshore (Figure 1a). The 136×250 point horizontal grid is specified in spherical polar coordinates with a uniform resolution of $5/128^\circ$ in longitude and $1/36^\circ$ in latitude, giving an average of approximately 3.1 km resolution within the domain. The Coriolis parameter varies with latitude. The vertical grid has 40 levels of terrain-following coordinate with enhanced resolution near the lower and especially upper boundaries specified by the stretching parameters $q_b=0.2$ and $q_s=6.0$ [*Song and Haidvogel*, 1994]. Bottom topography is a bilinear interpolation of ETOPO5 gridded data [*NGDC*, 1988] in deep waters offshore blended with high-resolution data that better represents details of the slope and shelf. Minimum water depth along the coast is fixed at 20 meters, but no limitation on maximum depth is imposed. Bottom slopes are smoothed to meet the r-factor criterion of 0.2, which reduces pressure gradient errors in terrain-following coordinates [*Beckmann and Haidvogel*, 1993].

2.2 Initial and boundary conditions

The coastline, which is represented as discrete stair steps, forms the closed eastern boundary where there is no normal flow and a free slip condition applies to tangential flow. The northern, southern, and

western edges are open boundaries. We use a *Chapman* [1985] condition on the free surface and a *Flather* [1976] condition on depth-averaged velocities normal to the open boundaries. The boundary condition applied to three-dimensional velocities and tracers is based on the radiation and nudging scheme described by *Gan and Allen* [2005b] with a modification for oblique radiation [*Marchesiello et al.*, 2001]. The nudging time scale is 100 days on outflow and 1 day on inflow. In a sponge layer at the open western and southern (but not northern) boundaries, the diffusivity and viscosity coefficients are set to 100 m²/s and tapered over 150 km to their interior values.

Data values for the initial and boundary conditions are derived from the Naval Research Laboratory NCOM-CCS model [*Shulman et al.*, 2004], which extends from 30° N to 49° N and from the coast to 135° W in spherical coordinates at 9-10 km resolution. The version used here did not assimilate data, but it was itself one-way nested in a data-assimilating 1/8° global model. Values for variables on the finer OCTZ grid are obtained by interpolation and, where required by differences in the bottom topography, extrapolation in a manner that maintains stable stratification. Boundary data are interpolated linearly in time between twice-daily snapshots. The simulation discussed here in detail is initialized with NCOM-CCS model output from the year 2001 on day 120 (May 1) and run through day 305 (November 1). Additional simulations are initialized on days 90, 100, 110, 130, and 140 to test sensitivity to initial conditions.

2.3 Forcing

Both NCOM-CCS and the OCTZ model are forced with the same wind stress, which was derived from the COAMPS [*Hodur*, 1997] Eastern Pacific reanalysis [*Kindle et al.*, 2002]. This data-assimilating, mesoscale, regional model reproduces spatial variation of the winds (Figure 2), including the orographically enhanced wind jet to the southwest of Cape Blanco that arises during upwelling-

favorable winds [Samelson *et al.*, 2002; Perlin *et al.*, 2004]. At the location of NOAA weather buoy 46050 (44.62° N 124.53° W; approximately 37 km off Newport, Oregon) the major features of the meridional wind stress time series are similar to those discussed in detail by Bane *et al.* [2005]. During the period from day 120 –305 the predominantly southward (70% of the time), upwelling-favorable nearshore winds were enhanced by approximately 12-16 major (southward wind speed exceeding 5 m s⁻¹) upwelling-favorable events and reversed by a similar number of briefer downwelling-favorable (northward wind) events (Figure 3). Zonal wind stress remained relatively small throughout the summer. Hourly COAMPS wind stress is boxcar-averaged to four-hour intervals and is bilinearly interpolated to the OCTZ grid to create forcing for the model.

The COAMPS model provides shortwave radiation, longwave radiation, latent, and sensible heat fluxes, which were used to force NCOM-CCS. The OCTZ model is also forced by the shortwave radiation component distributed over depth according to the profile associated with Jerlov water type 1 [Paulson and Simpson, 1977]. However, initial testing showed that the upper ocean was consistently cool if the other components (sensible, latent, longwave) of heat flux from COAMPS were used to force the OCTZ model; instead, these heat fluxes are calculated internally by ROMS using the bulk flux formulation of Fairall *et al.* [1996]. For this purpose, NCEP reanalysis values are used for air temperature, humidity, pressure, and cloud cover, as these were not available to us from COAMPS.

No freshwater or salinity flux through the ocean's surface is prescribed. River inflow is neglected, but some influence of freshwater sources enters through the initial and northern boundary conditions. Tidal forcing is not included. We consider the effects of the barotropic tide and the Columbia River plume elsewhere [Springer *et al.*, 2008].

2.4 Data

A variety of data is used for validating the OCTZ model simulations. NOAA tide gauges and TOPEX/Poseidon altimeters provide measurements of sea level (Figure 1a). Tide gauge data are demeaned with the average value for 2001, 40-hour low-pass filtered, and corrected for the inverse barometer effect [Barron *et al.*, 2004]. The TOPEX/Poseidon satellite measured sea surface height with a 10-day repeat cycle along four ground tracks, 247, 206, 171, and 28, in the time and region of interest. An absolute dynamic topography product, formed by combining the altimeter-measured anomalies with a mean sea surface topography from a geoid model, in situ density measurements, and multiple years of altimetry data [Rio and Hernandez, 2004], is used for the comparisons below. Because this sea level product has a different reference level from NCOM-CCS, a spatially averaged bias of 1.5 m is removed.

As part of the COAST program [Barth and Wheeler, 2005], detailed observations from summer 2001 were made in the region of Stonewall Bank and Heceta Bank, submarine topographic features along the central Oregon shelf extending alongshore from 44.1° N to 45.1° N and offshore to 125° W (Figure 1b). Available data include high frequency (HF) radar estimates of surface current [Kosro, 2005], moored observations of temperature, salinity, and ADCP-measured velocities [Boyd *et al.*, 2002], and high-resolution hydrographic sections [Barth *et al.*, 2005; Castelao and Barth, 2005]. Most of the moorings (NIS, NMS, NSB, SIS, SMS, SSB; see Figure 1b) were deployed from days 140-240, but a long term GLOBEC mooring (NH-10) was in place for the entire time period considered here. In cases in which the model and mooring bottom depth differ significantly, the model is sampled at a nearby location with a similar bottom depth, rather than the closest possible location. HF radar-measured current velocities were mapped on a 2 km grid, and, for comparisons, the modeled surface velocities are interpolated to the same grid. All mooring and HF radar data and the corresponding

model data are smoothed with a 40-hour low-pass filter to minimize tidal currents and inertial oscillations.

3. OCTZ simulations

3.1 Large-scale Circulation

The mean model sea-surface temperature, salinity, height, and currents over the simulation interval, days 120-305 of year 2001, show a region of cold, saline, low sea-surface elevation, and strong, generally southward flow over the shelf and slope (Figure 4). Cold surface temperatures and, especially, high surface salinities are more evident in the southern half of the domain. Some evidence of spurious boundary effects on sea surface temperature and height is suggested in the northwestern part of the domain, but these appear to be limited in amplitude and extent. Persistent offshore flow, extending from the shelf across the slope to the deep interior, occurs near the latitude of Cape Blanco, around 42.8° N (Figure 4d). Offshore extension of the low temperatures, high salinities, and low sea-surface heights are also evident at these southern latitudes (Figure 4a-c). The overall patterns of these mean surface variables are consistent with the coastal upwelling response to the mean upwelling-favorable wind stress during this period (Figure 2). The large cross-shore gradients over the shelf and slope are the mean expression of the coastal upwelling front, separating the cold, saline upwelled water inshore from the warm, fresh surface water offshore, and the large surface currents (up to 0.5 m/s) are the mean expression of the associated geostrophic coastal upwelling jets. Southward intensification of the mean upwelling response is consistent with the southward intensification of the mean wind stress over this region, including the orographic intensification associated with Cape Blanco [Perlin *et al.*, 2004].

A north-south difference in cross-shore location of the surface front, relative to the shelf and slope

topography, is evident in zonal cross-sections at 41.9° N, 43.21° N, and 44.65° N of the mean model temperature, salinity, and meridional currents (Figure 5). At the two northern sections the upwelling front occurs over the shelf, within the 200 m isobath, but it is farther away from the coast, over deep water, at the southern section. Isohalines and isotherms in the upper ocean slope upwards toward the coast, and the geostrophic, southward currents are limited to shallow depths. Beneath about 50-100 m the isotherms and isohalines slope downward onshore, consistent with a northward undercurrent that is found in relatively shallower water, with speed exceeding 0.1 m/s, at the southern section, but is deeper and weaker to the north. As the surface jet moves offshore near Cape Blanco, it crosses over the undercurrent, resulting in a relatively large mean vertical shear near 43.21° N. These features of the undercurrent agree qualitatively with observations [Pierce *et al.*, 2000]. A similar undercurrent is found in the NCOM-CCS model [Choboter *et al.*, 2006], and it passes to the OCTZ model through initial and boundary conditions.

The mean modeled sea surface height can be compared with absolute dynamic topography along several TOPEX/Poseidon tracks that cross the model domain averaged over the simulation time interval (Figure 6). (Note that such a long time average emphasizes the mean part of dynamic topography product rather than the time-dependent anomalies measured by satellite altimetry.) Along the tracks east of 127° W, the time-mean sea surface height drops by 0.1-0.2 meters over comparable cross-shore scales in both the observations and the simulation, demonstrating that the model has a realistic sea surface height gradient associated with the jet. West of 127° W, however, the modeled sea surface height gradient is weakened or reversed compared with the observations. Along tracks 206 and 171, the simulated sea level at the model's open western boundary is lower than observed by approximately 0.1 meters. This discrepancy arises from the low sea level imposed by the boundary conditions from NCOM-CCS. An additional shortcoming is that the model-simulated sea surface height is about 0.05 m

too high along the entirety of track 28.

The upwelling front and coastal jet evolve extensively over the course of the simulation. Early in the spring, the upwelling front and jet roughly follow the shelf break (200 m isobath, nominally). By day 171 (Figure 7a) the coastal jet separates from the 200 m isobath near the tip of Cape Blanco and follows a meandering path over deep water more than 100 km offshore. The meandering current forms an elongated loop that reaches more than 200 km offshore near 42° N by day 201 (Figure 7b) and detaches as an isolated eddy by day 261 (Fig 7d). Other, smaller eddies form near 44° N and 46° N during this period. These mesoscale features are poorly sampled by the sparse satellite coverage, but a general comparison of their scale and location is possible. On day 230, for example, the modeled and observed sea surface height features along track 247 have similar peak-to-trough amplitudes and alongtrack spatial scales (Figure 8a), and the model produces an offshore trough at nearly the correct location (Fig 7c). Along track 206 a sea-surface height front of similar magnitude is seen in both the model and observations, but it is several tens of kilometers farther offshore in the observations than in the model (Figure 8b). In general, the position of meanders or eddies along both tracks differs between the model simulation and the observations; however, in view of the fact that these features result from complex interactions, possibly due to instabilities, exact comparisons cannot be expected.

In addition to mesoscale variability, sea surface height in the OCTZ undergoes a domain-wide increase over the course of the model integration (Figure 7a-d). Since this gain is of large spatial scale, it can be evaluated by comparing modeled and observed sea surface height spatially averaged along TOPEX/Poseidon tracks (Figure 9). The model-simulated, alongtrack-averaged sea surface height along all four tracks shows a steady gain. Although the days of peak sea level differs among the tracks, they are generally consistent with the peak of the domain-averaged model-simulated increase, which occurs on day 272 at approximately 0.10 m higher than on day 120. Observed, alongtrack-averaged sea

levels show a similar trend and a similar summertime increase in dynamic height, attributable to seasonal heating, has been noted in this region [Huyer *et al.*, 2007]. Because the model reproduces the seasonal trend, correlations between the model and the observed alongtrack-mean height are high, but higher frequency variations, which are associated with mesoscale variability, are not well correlated and have larger amplitude in the observations than in the simulation.

In order to focus on the mesoscale variability, seasonal change in sea surface height is reduced by removing a linear temporal trend along each track. The spatial distributions of the temporal standard deviation of detrended sea surface height at each point along the tracks (Figure 10) are similar in the model and observations. The largest variability in both is concentrated west and south of the tip of Cape Blanco. Both the observations and the model simulation show enhanced variability southwest of Heceta Bank, but the model simulation also shows enhanced variability northwest of Heceta Bank that is not consistent with the observations. Overall, standard deviation of detrended sea surface height in the model simulation is smaller than in the satellite data.

Variability of other surface quantities is also enhanced in the region off Cape Blanco. Eddy kinetic energy (EKE), defined as $K' = \frac{1}{2}((u')^2 + (v')^2)$ where $(u', v') = (u, v) - (\bar{u}, \bar{v})$, and the overbar indicates a time average, is large over a region extending approximately 350 km to the southwest of the cape (Figure 11). (Note that the western and southern limits of this patch of EKE may be affected by the sponge layers with enhanced viscosity and diffusivity that lie along the western and southern boundaries.) This enhanced eddy kinetic energy lies along the path of the mean current as it separates from the coast (Figure 4d), so it can be interpreted as the time variability of the separated current. Eddy kinetic energy is also enhanced in regions over the shelf, particularly on the central Oregon coast. Calculation of geostrophic velocities from sea surface height (not shown) demonstrates that geostrophic flow accounts for nearly all of the eddy kinetic energy offshore but not all of the eddy kinetic energy

over the shelf.

3.2 Shelf circulation

Intensive observations along the central Oregon coast, 44.1° N to 45.1° N, make detailed model-data comparisons possible in this region of complex bottom topography. The mean (over days 140-240) model surface currents flow southward along the topographic contours to the west of Stonewall Bank and offshore on the northwest side of Heceta Bank (Figure 12b), leaving a region of weak currents on the inshore side of the bank. The HF-radar observed jet (Fig 12a) similarly follows the 80 m isobath and then crosses isobaths on the lee side of the bank [Kosro, 2005], but it is closer to shore and slightly weaker. After crossing isobaths, the model-simulated jet veers farther offshore so that the SMS mooring (Figure 1b) lies in the quiet region of the model rather than on the inshore edge of the jet as observed. Mean southward surface currents also lie adjacent to the coast, although in the model simulation these are too weak in the north and too strong in the south. As measured by standard deviation, speed in both the jet and the near shore region show more variability in the model than the HF radar measurements (Figure 12e). The amplitude of the complex correlation [Kundu and Allen, 1976] is high, and the phase angle is small, indicating that the timing and vector direction of the modeled and observed surface current variations are similar (Figure 12c). These correlations are greater than 0.7 near all of the mooring locations except SMS.

The flow of the jet is primarily in geostrophic balance, with smaller, but important, ageostrophic contributions [Gan and Allen, 2005a]. Calculation of dynamic height from high-resolution hydrographic sections and the model (not shown) result in a similar across-shore gradient from high values offshore to low values near the coast. Owing to the thermal wind balance, the strong surface velocities of the jet diminish with depth due the horizontal gradient in the density consistent with

upwelling of cold, saline water over the shelf. For example, during an episode of strong northerly winds (Figure 3) on days 219-221, zonal sections from the model show isotherms (Figure 13) and isohalines (not shown) sloping upward toward the coast and becoming nearly vertical in the mixed layer. The isotherms slope most strongly on the northern section, where the jet is close to shore, and more weakly on the southern section, where the jet is farther offshore and weaker. The observed isotherms slope similarly. Both the simulated and observed mixed layers are about 20 m deep, but the surface temperature is higher and the temperature gradient at the bottom of the mixed layer is much sharper in the observations. These deficiencies suggest that the model's surface heat flux formulation is supplying inadequate heat to the mixed layer.

The vertical structure of the temperatures and velocities can be compared quantitatively at the moorings. At NSB, for example, the model mean meridional velocity decreases from 0.35 m/s at the surface to 0 m/s at 90 m depth (Figure 14). In contrast, the standard deviation of model velocity is nearly independent of depth. The zonal velocity component at this location is weak in both the mean and in variability. The water column is temperature stratified, with large mean values and standard deviations of temperature confined to the upper 20 m. The model's meridional velocity has a depth-independent northward bias of approximately 0.03 m/s and larger standard deviation at all depths except near the bottom. Correlations of modeled and observed meridional velocity exceed 0.6 at all depths. The modeled and observed mean temperatures are close except in the upper 10 m, where the model is 1° C cooler than the observations, and the modeled standard deviation is roughly 70% of the observed. Correlations of modeled and observed temperature reach 0.8 in the upper ocean and are around 0.5 below 40 m.

Time series of near-surface temperatures at the moorings show the gradual increase of summertime mixed layer temperature due to surface heat flux modulated by cooling during upwelling events and

warming during downwelling events (Figure 15). Near-surface temperatures are generally warmer at the shelf break locations compared with the inner shelf locations, and peak between days 240 and 260. Modeled and observed surface temperatures have correlations ranging from 0.68 (over the longer time series at NH-10) to 0.92. The observed warming trend at NSB and SSB is not fully reproduced by the model, leading to root-mean-square (RMS) errors that reach 1.5-2° C. Near-bottom temperatures were relatively constant in both the model and observations.

Since fluctuations in the simulated velocities are largely independent of depth (e.g. Figure 14), we consider time series of depth-averaged velocities. To facilitate comparison with mooring observations, for which currents were not measured within 10-20 m of the top and bottom of the ocean, vertical averages for the model also exclude these regions. In addition, because fluctuations in depth-averaged currents at the moorings are strongly polarized, we rotated them to their principal axes of variation independently at each mooring. The orientation of the major axis of the simulated depth-averaged velocity is nearly meridional at most mooring locations, with a significant zonal component at SSB (Table 1), reflecting flow directed parallel to local isobaths. Owing to the dominant role of wind stress, depth-averaged, principal axis velocity fluctuations are largely coherent across the moorings, but there are spatial variations in the amplitude with higher speeds at the northern moorings than the southern moorings and inshore relative to offshore (Figure 16). In addition to the several-day time scale of wind-driven fluctuations, speed has a trend, decreasing by day 240 at all moorings and continuing to be weak until day 305 at NH-10. These general features are consistent with observations. The orientation of the major axis for the model velocities is within 7° of the observed at all moorings except NIS, possibly due to errors in the nearshore bathymetry (Table 1). Excluding SMS, where the weak flow is poorly simulated, correlations exceed 0.76 and RMS errors are less than 0.09 m/s. Dividing by the root mean square of the observed velocities gives normalized RMS errors (NRMSE), a measure of model skill,

with smaller values along the northern line of moorings and larger values along the southern line.

Compared with the major axis velocities, the minor axis velocity means and standard deviations (Table 2) are small (generally less than .01 m/s and .02 m/s, respectively) in both the simulation and the observations. The cross-correlations of these signals is near zero and the normalized RMS errors exceed one; together, these measures indicate that the model does a poor job of simulating the weak velocities that correspond roughly to across-shelf flow.

Tide gauge data gives some idea of the variability along the coastline in areas other than the Heceta Bank region. Comparison of time series of the model-simulated sea level and wind-stress shows wind-forced features are highly correlated along the coast (Figure 17). The amplitude of the modeled sea level fluctuations increases from south to north, and, in addition, a trend in sea level occurs over the time period of the model integration, most evidently at North Spit, the southernmost location. Both the long and short time scale changes accurately reflect changes in observed sea level, although there is a model bias of about 0.02 m at most locations and 0.07 m at Toke Point. Without this bias, RMS errors would be 0.03-0.05 m. Correlations of modeled and observed coastal sea level are 0.87-0.89 at all tide gauges except Astoria, a sheltered estuarine location.

4. Discussion

4.1 Comparison with previous model simulations

A number of previous numerical modeling studies have simulated circulation on the central Oregon shelf [*Oke et al.*, 2002 a,b; *Kurapov et al.*, 2005 a,b; *Gan and Allen*, 2005a]. *Gan and Allen* [2005a], in particular, simulated the Heceta Bank region over the first half of the time interval used here. Although the results are not directly comparable because of the difference in time period, their depth-averaged velocity correlations in the mooring array were all less than 0.7, and the RMS errors were 0.03-0.05

m/s larger than those given here. Correlations and errors in the temperatures at the moorings were comparable to those found here. In a similar model of the same region and same time period, *Kurapov et al.* [2005b] demonstrated other deficiencies in model coastal sea level, surface velocities, and stratification. They showed that assimilating mooring velocities improved the model accuracy. After assimilation, the statistics of their comparisons were similar to those obtained by the non-assimilating model OCTZ presented here.

Major limitations of these previous models were the use periodic conditions on the northern and southern boundaries and the use of spatially uniform winds. To address these issues *Gan et al.* [2005] applied open boundary conditions at the northern and southern boundaries and forced the model with spatially variable winds from a mesoscale atmospheric model [*Samelson et al.*, 2002]. Improvements in the simulation of amplitude and phase of velocities measured at the moorings were attributed (without demonstration) to coastal trapped waves generated by enhanced strength and variability of wind stress south of Cape Blanco [*Perlin et al.*, 2004]. Because the southern boundary condition was determined by solutions to a two-dimensional (zonal slice) model, no coastal-trapped waves propagated into the domain from the south.

4.2 Coastal trapped waves

Exploring the role of coastal-trapped waves (CTW) on the circulation on the central Oregon shelf helps differentiate the relative importance of wind within the domain and wind south of the domain acting through the open boundary conditions. Sub-tidal variation in sea level along the western coast of North America can be usefully modeled [*Halliwell and Allen*, 1984; *Battisti and Hickey*, 1984] by a forced and damped, one-dimensional wave equation

$$\frac{1}{c_n} \frac{\partial Y_n}{\partial t} + \frac{\partial Y_n}{\partial y} + \frac{Y_n}{c_n T_f} = b_n \tau(y, t). \quad (1)$$

For each shelf mode n , Y_n represents coastal sea level, c_n is the phase speed, b_n is the projection of the alongshore wind stress, τ , onto the mode, and T_f is a frictional damping time scale. For comparison with the model simulations we computed solutions to (1) with forcing τ from the meridional COAMPS wind stress averaged over a 50 km strip adjacent to the coast and a southern boundary condition from NCOM-CCS coastal sea level at 40.5° N. Following *Halliwell and Allen* [1984], we used a single mode with $c_I = 3.25 \text{ m s}^{-1}$, $T_f = 4.25 \text{ days}$, and $b_I = 1.19 \times 10^{-6} (\text{N m}^{-2})^{-1}$.

The CTW model explains most of the variance in coastal sea level. At the South Beach tide gauge (Figure 1b), it reproduces sea level variability as well as the OCTZ model (Figure 18a). As in the OCTZ model, cross correlations between the CTW model and observations are larger and RMS differences are smaller in the southern half of the domain, but these statistics degrade more abruptly for the CTW model than the OCTZ model in the northern part of the domain (Table 3). By these measures, the OCTZ model and the wave model are more similar to one another than either is to the observations, so it is sensible to use the wave model to interpret the OCTZ model.

In particular, the simplicity of the CTW model makes it possible to separate the effects of boundary conditions and regional forcing on the coastal sea level by varying the boundary conditions or forcing only in restricted regions. Such an analysis shows that, at the South Beach tide gauge (Figure 18b), the trend arises mostly from the southern boundary condition, meaning that it results from changes in sea level outside the OCTZ domain. Although the boundary condition contributes at the frequencies of wind variability, the largest part of the signal results from orographically intensified winds within the domain, between 40.5° N and 42.75° N. Additional wind forcing between 42.75° N and the tide gauge enhances the signal further. The contributions of these various components of the signal can be

quantified by the percent of observed variance explained after demeaning the time series. At South Beach, the southern boundary condition contribution is 53%, the boundary condition plus forcing to 42.75° N is 77%, and the total wave model, including forcing between 42.75° N and the location of the South Beach tide gauge is 73%, a slight degradation. At tide gauges farther to the north, the contribution of the southern boundary condition becomes less important and the winds north of Cape Blanco become more important (not shown). The worsening of the representation of sea level in the northern part of the domain may be due to errors in the wind stress north of South Beach or to spatial variability in the appropriate parameters for the wave model.

A CTW model can also be applied to velocities [*Battisti and Hickey, 1984*] and compared with the observed and OCTZ-modeled principal-axis, vertically averaged velocities defined above. To do so, estimates of the cross-shelf structure of the CTW modes must be obtained. Because of the complex topography in the Heceta Bank region, we did not use a dynamical CTW mode but instead we used the first mode of a multivariate EOF analysis (not shown) of the OCTZ model output. The relative weights of this EOF at the mooring locations (Table 4) are generally consistent with the expected dynamical mode structure, with stronger weighting closer to shore and at the northern mooring line, where the shelf is relatively narrow. Additional free parameters in the CTW equation for velocity are a scaling factor for the conversion of pressure to velocity, and the weighting of the boundary condition. These parameters were selected here, within reasonable bounds, to fit the observations. The boundary condition is the vertically averaged meridional velocity on the 100 m isobath at the southern boundary. Unlike the case for sea level, this velocity boundary condition shows no trend, and the wave model does not explain the trend in velocity noted earlier. For this reason, the temporal trend is removed from the observed data and OCTZ model data for comparison with the wave model predictions.

At the frequency of wind events, the velocity comparison at NH-10 is similar to the coastal sea

level comparison at South Beach (Figure 18c). On several occasions during the middle of the summer, the observed velocities did not respond as strongly to upwelling favorable winds as predicted by the wave model, although coastal sea level did. An analysis of the contributions to the wave amplitude for velocities yields different results than for sea level. Without a long-term trend, the contribution of the southern boundary condition to the depth-averaged velocity variance is much smaller (Figure 18d), explaining 8% of the observed variance at NH-10. This result suggests that freely propagating waves originating south of Cape Mendocino play a small role in velocity fluctuations on the central Oregon coast. The boundary condition plus the forcing south of Cape Blanco explains 50% of the observed variance, indicating that the orographically enhanced winds in this region have an important effect on the velocities near Heceta Bank. Adding the forcing north of Cape Blanco increases the percent of observed variance explained to 53%, so the winds between 42.75° N and 44.65° N, the latitude of the mooring, contribute relatively little. Because of the similarity of the wave model and OCTZ model predictions for velocity (Table 4), the relative importance of these contributions is probably similar in the OCTZ model.

4.3 Lagrangian pathways from shelf to open ocean

The present simulation resolves a broad range of shelf, slope, and offshore scales of motions, and provides a new opportunity to investigate the complex three-dimensional Lagrangian motions that are associated with the coastal upwelling circulation and the interaction of shelf-scale processes with the slope and interior. In addition to their intrinsic physical interest, these Lagrangian pathways are of particular importance for biological processes and ecosystem dynamics. We focus here on one specific aspect of this problem: the origin of the waters that form the meanders and eddies offshore of Cape Blanco.

The active tracers in the model, temperature and salinity, indicate the location of upwelled water, but they do not show where or when it upwelled. For this purpose, it is useful to define Lagrangian labels $X(x, y, z, t)$, $Y(x, y, z, t)$, and $Z(x, y, z, t)$, satisfying the following equations:

$$\frac{DX}{Dt} = 0, \frac{DY}{Dt} = 0, \frac{DZ}{Dt} = 0, \quad (2)$$

where $D/Dt = \partial/\partial t + u\partial/\partial x + v\partial/\partial y + w\partial/\partial z$. With the initial conditions at $t=t_0$

$$X(x, y, z, t_0) = 0, Y(x, y, z, t_0) = 0, Z(x, y, z, t_0) = 0, \quad (3)$$

these labels give, respectively, the initial x , y , and z (longitude, latitude, and depth) locations of the parcels that are found at positions (x, y, z) at time t [Kuebel, Cervantes, and Allen, 2006]. The evolution of the label fields is calculated on the model grid at every time step using the same horizontal and vertical advection schemes used for temperature and salinity. However, the label tracers are not subject to diffusion; thus, the interpretation of these Lagrangian labels can be ambiguous if the inferred trajectories pass through regions of strong turbulent mixing, such as the surface and bottom boundary layers over the shelf, where mixing alters the identity of water parcels.

Lagrangian labels help identify the pathways of water parcels during the strong, upwelling-favorable winds that dominate from day 190 to day 210 (Figure 3). The label fields are initialized on day 190 [$t_0=190$ in (3)], and (2) is integrated as part of the model simulation to day 210. At any location on the final day, the initial position can be determined by examining the Lagrangian label. For example, water located at the sea surface south of Cape Blanco on day 210 that originated north of 44° N, say, can be identified, and its initial and final positions mapped (Figure 19). The results suggest that this fluid originates over the Heceta Bank region and over the northern Oregon shelf and slope, and that the inshore portion of fluid has upwelled from depths of 50 to 80 m, while the offshore portion originated at the surface on day 190. Overall, the label calculation indicates that the fluid at the surface on day

210 that has upwelled from depths greater than 20 m on day 190 is primarily found on day 210 over the southern shelf and slope, south of Cape Blanco, and extending offshore past 126° W (Figure 20).

These inferences about relationship between the shelf circulation and the separated current south of Cape Blanco are qualitatively consistent with observations. Surface drifters deployed over the shelf along 44.65° N during July of 2000-2003 moved southward in the coastal jet and followed it offshore near Cape Blanco [Barth, 2003]. Isopycnal floats deployed beneath the mixed layer north of Heceta Bank in 2000 and 2001 also moved generally southward [D'Asaro, 2004]. Some were advected onshore and upward, consistent with upwelling, while others followed a path around the outer edge of Heceta Bank and reached the surface near Cape Blanco.

4.4 Effects of perturbed initial conditions

The significance of detailed model-data comparisons presented earlier depends in part on the predictability of the flow. Here we test sensitivity to initial conditions by considering a small ensemble consisting of the original simulation plus four additional simulations that are initialized from NCOM-CCS 10 and 20 days earlier and later.

The effect of the perturbation in initial conditions on the solutions varies spatially. Differences between sea surface height in model runs in the ensemble are small on the shelf; for example, at each tide gauge correlations vary by less than 0.06 and RMS errors relative to observations vary by less than 0.008 meters between ensemble members (Table 5). For depth-averaged velocities, differences in correlations tend to be smaller closer to shore and larger toward the shelf break (Table 6). Seaward of the 200 meter isobath, differences between the model runs grow over time, and the divergence of the solutions is quantified by the ensemble standard deviation of sea surface height (Figure 21). On day 170 the differences begin in a small region primarily west of Cape Blanco and Heceta Bank as

deviations in the path of the coastal jet, and over time large values of ensemble standard deviation spreads northward and westward. The peak value of 0.12 meters occurs on day 260 (Figure 21d) and represents differences in the position of the large cyclonic eddy, which is recognizable in all members of the ensemble but occurs in different locations to the southwest of Cape Blanco. The domain-averaged ensemble standard deviation in sea surface height grows at a nearly linear rate throughout the course of the integration, increasing from 0.005 meters on day 140 to 0.025 meters on day 305.

Although details of the circulation are affected by the initial conditions, the differences between model runs are localized and can be minimized by averaging over space. This localization is demonstrated by considering the surface total kinetic energy in three regions: a coastal region east of 125° W, a southern offshore region west of 125° W and south of 43.5° N, and a northern offshore region west of 125° W and north of 43.5° N. Differences in surface total kinetic energy averaged over the coastal region are small until after day 200, and are always much smaller than the fluctuations in the ensemble mean (Figure 22), indicating that the shelf flow is strongly controlled by the wind forcing. In the southern offshore region, which lies west of Cape Blanco, all model runs in the ensemble show a similar increase in average kinetic energy from initialization to roughly day 200-210, followed by a slow decrease, with relatively little indication of direct response to wind variability. The ensemble spread is initially small but expands around day 180 and stays constant thereafter. The northern region has lower surface kinetic energy, which increases only slowly over the simulations, and ensemble standard deviations remain small. Although the precise time and location of mesoscale features is unpredictable, the seasonal peak and the general location in a region west of Cape Blanco and south of Heceta Bank are robust characteristics.

5. Conclusions

The present OCTZ simulation reproduces accurately the detailed structure of the shelf flow over the region of complicated topography of Heceta Bank along the central Oregon coast. These flows are mediated in part by coastal trapped wave processes that span the south model boundary. At the same time, it provides a representation of jet separation and eddy formation in the OCTZ, especially off Cape Blanco, in approximate accord with available observations. The Lagrangian label tracer calculations allow the identification of the source of upwelled water in the separated jet and eddy features off Cape Blanco, a first step in the modeling and analysis of the cross-shelf exchange of fluid and material that controls the characteristics of the northernmost portion of the California Current System. The ensemble calculations, although limited in scope, suggest that the variability in the Cape Blanco region is a mixture of deterministic response to wind forcing and intrinsic instability of the separated jet.

Some of the improvements relative to previous models of this region resulted from the nested boundary conditions. Earlier models of the central Oregon shelf were limited by their use of periodic boundary conditions, which did not allow propagation of coastal trapped waves or advection of tracers into or out of the domain. We showed that these waves have an effect on the long-term sea level and a lesser effect on the vertically averaged velocities. The effects of nesting on other features of the circulation, such as the existence and strength of the coastal undercurrent, are more complex and await further analysis.

Improvement of simulated circulation over the shelf also resulted from using wind stress forcing that is highly resolved in both time and space. Most of the earlier models of the Oregon shelf used spatially uniform winds with values obtained from a single measurement point, which gave high temporal resolution but no spatial resolution. Analysis of a coastal trapped wave model shows that variability in depth-averaged velocities and sea level near Heceta Bank result less from fluctuations in

local winds than from fluctuations in orographically enhanced wind stress south of Cape Blanco. These winds also cause upwelling south of the cape that contributes to the low temperature, high salinity surface waters that appear inshore of the coastal jet after it has separated. Detailed Lagrangian circulation analysis covering more upwelling events than are considered here will help quantify the relative importance of upwelling south of Cape Blanco, between Cape Blanco and Heceta Bank, and over Heceta Bank in the formation of this pool. Some of this upwelled water is incorporated into mesoscale eddies that carry it farther offshore.

The divergence of model simulations in the ensemble experiments shows that the evolution of the circulation is not strictly deterministic. The magnitude of difference between ensemble members depends on spatial location. Coastal sea level is almost unaffected while in the mid- and outer-shelf regions on the central Oregon coast, vertically averaged velocities are somewhat affected by changes in the position and strength of the coastal jet related to the perturbations. Larger differences appear in mesoscale features off the shelf, so that the exact position of a coastal jet meander or an eddy differs between model runs in the ensemble, but even these differences are limited both geographically and temporally. The results of this small ensemble suggest that model data comparisons in the region off Cape Blanco are best limited to statistical rather than detailed point-by-point comparisons.

Differences from observed data revealed shortcomings of the nested grid model simulations. The most serious discrepancy is that the mean sea surface height in the northern part of the domain differs considerably from the absolute dynamic topography product. Owing to the boundary conditions used here, sea surface height on the boundary of the nested model nearly matches that of the model in which it is nested; thus, errors in the large-scale sea surface height of the OCTZ model are due in part to errors in the non-assimilating NCOM-CCS model. Experiments with nesting in a version of NCOM that assimilates upper ocean density shows some improvement in this regard. Another difficulty is that

the sea surface temperature in offshore areas consistently is too high by about 2° C while over the shelf it tends to remain too low. Efforts to improve the surface heat flux in the OCTZ model are under way.

Acknowledgments

Computer time was provided by Arctic Region Supercomputing Center. Jianping Gan provided code for the implementation of boundary conditions. S. deRada provided the NCOM-CCS model output. The COAST mooring data were provided by M. Levine, T. Boyd, and M. Kosro, the NH-10 mooring data and HF radar data were provided by P. M. Kosro, the Seasor sections were provided by J. Barth. The altimeter products were produced by Ssalto/Duacs and distributed by Aviso, with support from CNES. This research was supported by the U.S. Office of Naval Research, Grant N00014-05-1-0891 through the National Ocean Partnership Program.

References

Bane, J. M., M. D. Levine, R. M. Samelson, S. M. Haines, M. F. Meaux, N. Perlin, P. M. Kosro, and T. Boyd (2005), Atmospheric forcing of the Oregon coastal ocean during the 2001 upwelling season. *J. Geophys. Res.*, *110*, C10S02, doi:10.1029/2004JC002653.

Barron, C.N., A. Birol Kara, H.E. Hurlburt, C. Rowley, and L.F. Smedstad (2004), Sea surface height predictions from the global Navy Coastal Ocean Model during 1998–2001. *J. Atmos. Oceanic Technol.*, *21*, 1876–1893.

Barth, J.A. (2003), Anomalous southward advection during 2002 in the northern California Current: Evidence from Lagrangian surface drifters. *Geophysical Research Letters*, *30*(15), 8024, doi:10.1029/2003GL017511.

Barth, J. A., S.D. Pierce, and R.L. Smith (2000), A separating coastal upwelling jet at Cape Blanco, Oregon, and its connection to the California Current System. *Deep-Sea Res. II*, *47*, 783–810.

Barth, J. A., and P. A. Wheeler (2005), Introduction to special section: Coastal Advances in Shelf Transport. *J. Geophys. Res.*, *110*, C10S01, doi:10.1029/2005JC003124.

Barth, J. A., S. D. Pierce, and R. M. Castelao (2005), Time-dependent, wind-driven flow over a shallow midshelf submarine bank. *J. Geophys. Res.*, *110*, C10S05, doi:10.1029/2004JC002761.

Batteen, M.L. (1997), Wind-forced modeling studies of currents, meanders, and eddies in the California Current System. *J. Geophys. Res.*, *102*, 985–1010.

Battisti, D.S., and B.M. Hickey (1984), Application of Remote Wind-Forced Coastal Trapped Wave Theory to the Oregon and Washington Coasts. *J. Phys. Oceanogr.*, *14*, 887–903.

Beckmann, A., and D.B. Haidvogel (1993), Numerical Simulation of Flow around a Tall Isolated

Seamount. Part I: Problem Formulation and Model Accuracy. *J. Phys. Oceanogr.*, 23, 1736–1753.

Boyd, T. J., M. D. Levine, P. M. Kosro, S. R. Gard, and W. Waldorf (2002), Observations from moorings on the Oregon Continental Shelf, May August 2001, Data Rep. 190, Ref. 02-6, Coll. of Oceanic and Atmos. Sci., Oreg. State Univ., Corvallis. State Univ., Corvallis.

Brink, K.H., and T.J. Cowles (1991), The coastal transition zone program. *J. Geophys. Res.*, 96, 14637–14647.

Castelao, R. M., and J. A. Barth (2005), Coastal ocean response to summer upwelling favorable winds in a region of alongshore bottom topography variations off Oregon, *J. Geophys. Res.*, 110, C10S04, doi:10.1029/2004JC002409.

Chapman, D.C. (1985), Numerical Treatment of Cross-Shelf Open Boundaries in a Barotropic Coastal Ocean Model. *J. Phys. Oceanogr.*, 15, 1060–1075.

Choboter, P. F., J. S. Allen, R. M. Samelson, and J. C. Kindle (2006), Dynamics of the California Undercurrent in th Navy Coastal Ocean Model. *Eos. Trans AGU*, 87(36), Ocean Sci. Meet. Suppl., Abstract OS-36G-15.

D'Asaro, E. (2004), Lagrangian trajectories on the Oregon shelf during upwelling. *Continental Shelf Research*, 24, 1421-1436.

Dinniman, M.S., and J.M. Klinck (2002), The Influence of Open versus Periodic Alongshore Boundaries on Circulation near Submarine Canyons. *J. Atmos. Oceanic Technol.*, 19, 1722–1737.

Fairall, C. W., E. F. Bradley, D. P. Rogers, J. B. Edson, and G. S. Young (1996), Bulk parameterization of air-sea fluxes for Tropical Ocean-Global Atmosphere Coupled-Ocean Atmosphere Response Experiment. *J. Geophys. Res.*, 101, 3747–3764.

Flather, R. A. (1976), A tidal model of the north-west European continental shelf. *Mem. Soc. R. Sci.*

Liège 6 série, 10, 141-164.

Gan, J. and J. S. Allen (2005a), Modeling upwelling circulation off the Oregon coast, *J. Geophys. Res.*, 110, C10S07, doi:10.1029/2004JC002692.

Gan, J. P. and J.S. Allen (2005b), On open boundary conditions for a limited-area coastal model off Oregon. Part 1: Response to idealized wind forcing, *Ocean Modell.*, 8, 115—133.

Gan, J. P., J.S. Allen, and R.M. Samelson (2005), On open boundary conditions for a limited-area coastal model off Oregon. Part 2: Response to wind forcing from regional mesoscale atmospheric model, *Ocean Modell.*, 8, 155—173.

Haidvogel, D.B., H. Arango, W.P. Budgell, B.D. Cornuelle, E. Curchitser, E. Di Lorenzo, K. Fennel, W.R. Geyer, A.J. Hermann, L. Lanerolle, J. Levin, J.C. McWilliams, A.J. Miller, A.M. Moore, T.M. Powell, A.F. Shchepetkin, C.R. Sherwood, R.P. Signell, J.C. Warner, J. Wilkin (2007), Ocean forecasting in terrain-following coordinates: Formulation and skill assessment of the Regional Ocean Modeling System. *J. Comput. Phys.*, in press, doi:10.1016/j.jcp.2007.06.016

Halliwell, G. R. and J.S. Allen (1984), Large-scale sea level response to atmospheric forcing along the west coast of North America, summer 1973. *J. Phys. Oceanogr.*, 14, 864—886.

Hodur, R.M. (1997), The Naval Research Laboratory's Coupled Ocean/Atmosphere Mesoscale Prediction System (COAMPS). *Mon. Wea. Rev.*, 125, 1414—1430.

Huyer, A. (1983), Coastal upwelling in the California Current System. *Prog. Oceanogr.*, 12, 259-284.

Huyer, A., P.A. Wheeler, P. T. Strub, R. L. Smith, R. Letelier, and P. M. Kosro (2007), The Newport line off Oregon – Studies in the north east Pacific. *Prog. Oceanogr.*, 75, 126-160.

Kindle, J.C., R.M. Hodur, S. deRada, J.D. Paduan, L.K. Rosenfeld, F.Q. Chavez (2002), A COAMPS™ reanalysis for the Eastern Pacific: Properties of the diurnal sea breeze along the central California

coast. *Geophysical Research Letters*, 29, 56-61, DOI 10.1029/2002GL015566.

Kosro, P. M. (2005), On the spatial structure of coastal circulation off Newport, Oregon, during spring and summer 2001 in a region of varying shelf width. *J. Geophys. Res.*, 110, C10S06, doi:10.1029/2004JC002769.

Kuebel Cervantes, B. T., and J. S. Allen (2006), Numerical model simulations of shelf flows off northern California. *Deep Sea Res. II*, 53, 2956-2984.

Kundu, P. K., and J.S. Allen (1976), Some three-dimensional characteristics of low-frequency current fluctuations near the Oregon coast. *J. Phys. Oceanogr.*, 6, 181—199.

Kurapov, A. K., J. S. Allen, G. D. Egbert, and R. N. Miller (2005a) Modeling bottom mixed layer variability on the mid-Oregon shelf during summer upwelling. *J. Phys. Oceanogr.*, 35, 1629-1649.

Kurapov, A. K., J. S. Allen, G. D. Egbert, R. N. Miller, P. M. Kosro, M. Levine, and T. Boyd (2005b), Distant effects of assimilation of moored currents into a model of coastal wind-drive circulation off Oregon. *J. Geophys. Res.*, 110, doi:10.1029/2003JC002195.

Kurapov, A. K., J. S. Allen, G. D. Egbert, R. N. Miller, P. M. Kosro, M. Levine, and T. Boyd (2005c) Assimilation of moored velocity data into a model of coastal wind-drive circulation off Oregon: Multivariate capabilities. *J. Geophys. Res.*, 110, doi:10.1029/2004JC002493.

Marchesiello, P., J.C. McWilliams, A. Shchepetkin (2001), Open boundary conditions for long-term integrations of regional oceanic models. *Ocean Modell.*, 3, 1-20.

Marchesiello, P., J.C. McWilliams, and A. Shchepetkin (2003), Equilibrium Structure and Dynamics of the California Current System. *J. Phys. Oceanogr.*, 33, 753-783.

Mellor, G. L. and T. Yamada (1982), Development of a turbulence closure model for geophysical fluid

problems. *Rev. Geophys.*, 20, 851-875.

NGDC (1988), Data Announcement 88-MGG-02, Digital relief of the Surface of the Earth. NOAA, National Geophysical Data Center, Boulder, Colorado.

Oke, P. R., J. S. Allen, R. N. Miller, G. D. Egbert, J. A. Austin, J. A. Barth, T. J. Boyd, P. M. Kosro, and M. D. Levine (2002a), A modeling study of the three-dimensional continental shelf circulation off Oregon. Part I: model-data Comparisons. *J. Phys. Oceanogr.*, 32, 1360—1382.

Oke, P. R., J. S. Allen, R. N. Miller, and G. D. Egbert (2002b), A modeling study of the three-dimensional continental shelf circulation off Oregon. Part II: dynamical analysis. *J. Phys. Oceanogr.*, 32, 1383—1403.

Paulson, C.A., and J.J. Simpson (1977), Irradiance Measurements in the Upper Ocean. *J. Phys. Oceanogr.*, 7, 952—956.

Perlin, N., R.M. Samelson, and D.B. Chelton (2004), Scatterometer and Model Wind and Wind Stress in the Oregon–Northern California Coastal Zone. *Mon. Wea. Rev.*, 132, 2110–2129.

Pierce, S. L., R.L. Smith, P.M. Kosro, J.A. Barth, and C.D. Wilson (2000), Continuity of the poleward undercurrent along the eastern boundary of the mid-latitude north Pacific. *Deep-Sea Res. II*, 47, 811-829.

Powell, T. P., C. V. W. Lewis, E. N. Curchitser, D. B. Haidvogel, A. J. Hermann, and E. L. Dobbins (2006), Results from a three-dimensional, nested biological-physical model of the California Current System and comparisons with statistics from satellite imagery, *J. Geophys. Res.*, 111, C07018, doi:10.1029/2004JC002506.

Rio M.-H., F. Hernandez (2004), A mean dynamic topography computed over the world ocean from altimetry, in situ measurements, and a geoid model, *J. Geophys. Res.*, 109, C12032,

doi:10.1029/2003JC002226.

Samelson, R., P. Barbour, J. Barth, S. Bielli, T. Boyd, D. Chelton, P. Kosro, M. Levine, E. Skillingstad, and J. Wilczak (2002), Wind stress forcing of the Oregon coastal ocean during the 1999 upwelling season, *J. Geophys. Res.*, 107(C5), 3034, doi:10.1029/2001JC000900.

Shchepetkin, A. F., and J. C. McWilliams (2003), A method for computing horizontal pressure-gradient force in an oceanic model with a nonaligned vertical coordinate, *J. Geophys. Res.*, 108(C3), 3090, doi:10.1029/2001JC001047.

Shchepetkin, A. F., and J.C. McWilliams (2005), The regional oceanic modeling system (ROMS): a split-explicit, free-surface, topography-following-coordinate oceanic model. *Ocean Model.*, 9, 347-404.

Shulman, I., J.C. Kindle, S. deRada, S.C. Anderson, B. Penta, and P.J. Martin (2004), Development of a Hierarchy of Nested Models to Study the California Current System. *Estuarine and Coastal Modeling 2003, Estuarine and Coastal Modeling, 8th International Conference on Estuarine and Coastal Modeling*, Malcolm L. Spaulding - Editor, November 3–5, 2003, Monterey, California, USA.

Song, Y., D. Haidvogel (1994): A semi-implicit ocean circulation model using a generalized topography-following coordinate system. *J. Comput. Phys.*, 115, 228-244.

Springer, S.R., A.K. Kurapov, D. Fulton, J.S. Allen, B.M. Hickey, J. Barth, and M. Kosro (2008), Dynamical effects of the Columbia River plume off the coast of Oregon. In preparation.

Strub, P.T. and C. James (2000), Altimeter-derived variability of surface velocities in the California Current System: 2. Seasonal circulation and eddy statistics, *Deep-Sea Res. II*, 47, 831-870.

Wijesekera, H. W., J. S. Allen, and P. A. Newberger (2003), Modeling study of turbulent mixing over

the continental shelf: Comparison of turbulent closure schemes, *J. Geophys. Res.*, 108(C3), 3103,
doi:10.1029/2001JC001234.

Mooring Location	Model			Observation			Comparison		
	Mean	Std. Dev.	Angle	Mean	Std. Dev	Angle	Correlation	RMSE	NRMSE
SSB	-0.084	0.085	28	-0.040	0.066	21	0.85	0.063	0.809
SMS	0.016	0.038	1.7	-0.040	0.068	8.7	0.40	0.085	1.074
SIS	-0.067	0.089	5.2	-0.015	0.091	2.3	0.76	0.081	0.872
NSB	-0.087	0.121	8.4	-0.120	0.102	9.0	0.81	0.079	0.500
NMS	-0.139	0.145	-0.61	-0.141	0.157	8.0	0.90	0.067	0.320
NIS	-0.138	0.147	-5.0	-0.109	0.168	8.8	0.88	0.085	0.423
NH-10	-0.094	0.132	21.2	-0.148	0.133	24.4	0.85	0.089	0.450

Table 1: Statistical properties of the major axis variations of depth-averaged velocities (see text for definition) at the mooring locations. Units of mean, standard deviation, and root mean square error (RMSE) are ms^{-1} and angles are degrees counterclockwise from north. Normalized root mean square (NRMSE) is defined as RMSE divided by the root mean square amplitude of the observed velocity signal.

Mooring Location	Model		Observation		Comparison		
	Mean	Std. Dev.	Mean	Std. Dev	Correlation	RMSE	NRMSE
SSB	0.004	0.017	-0.008	0.018	0.16	0.026	1.294
SMS	-0.007	0.022	0.001	0.041	0.04	0.046	1.137
SIS	-0.001	0.014	-0.018	0.017	0.04	0.027	1.118
NSB	0.006	0.012	-0.004	0.015	-0.12	0.023	1.485
NMS	0.008	0.018	-0.001	0.020	0.01	0.028	1.438
NIS	0.009	0.021	-0.010	0.014	-0.03	0.032	1.834
NH-10	0.002	0.015	-0.006	0.028	0.27	0.029	1.019

Table 2: Statistical properties of the minor axis depth-averaged velocities at the mooring locations. Definitions and units are as indicated in Table 1.

Tide gauge	Lat. (°N)	ROMS vs. Obs		CTW vs. Obs.		CTW vs. ROMS at tide gauge locations	
		Corr.	RMSE	Corr.	RMSE	Corr.	RMSE
Toke Point	46.71	0.87	0.09	0.56	0.09	0.83	0.05
Astoria	46.21	0.73	0.06	0.47	0.06	0.86	0.05
South Beach	44.63	0.89	0.03	0.83	0.03	0.92	0.03
Charleston	43.35	0.88	0.03	0.88	0.02	0.94	0.02
Crescent C.	41.75	0.89	0.04	0.87	0.03	0.94	0.02
North Spit	40.77	0.88	0.04	0.90	0.03	0.92	0.02

Table 3: Statistical properties of sea level in the OTCZ model (ROMS) compared with tide gauge observations (Obs.), the one-dimensional wave model (CTW) compared with tide gauge observations (Obs.) and ROMS compared with CTW modeled sea level. RMSE is root mean square error (meters) and Corr. is correlation coefficient.

Mooring Location	EOF Weight	ROMS vs. Obs.		CTW vs. Obs.		CTW vs. ROMS	
		Corr.	SDE	Corr.	SDE	Corr.	SDE
NSB	0.7192	0.76	0.04	0.88	0.05	0.88	0.05
NMS	1.0000	0.89	0.06	0.88	0.07	0.91	0.06
NIS	1.0495	0.87	0.06	0.81	0.10	0.87	0.08
NH-10	0.6481	0.79	0.07	0.78	0.06	0.76	0.07
SSB	0.3222	0.83	0.06	0.72	0.04	0.85	0.03
SMS	0.0651	0.31	0.08	0.21	0.05	0.21	0.04
SIS	0.6692	0.76	0.07	0.58	0.09	0.80	0.06

Table 4: Statistical properties of detrended principal axis velocities in the OTCZ model (ROMS) compared with those at the moorings (Obs.) (these differ from the numbers in Table 1 because the trend has been removed), the one-dimensional wave model (CTW) compared with tide gauge observations (Obs.) and ROMS compared with CTW modeled sea level. STDE is standard deviation of error (ms^{-1}), which is root mean square error after the mean is removed, and Corr. is correlation coefficient.

	Toke Pt.		Astoria		South Beach		Charleston		Crescent C.		North Spit	
	Min.	Max.	Min.	Max.	Min.	Max.	Min.	Max.	Min.	Max.	Min.	Max.
Correlation	0.86	0.87	0.68	0.74	0.86	0.89	0.86	0.89	0.86	0.89	0.84	0.89
RMSE	0.049	0.052	0.043	0.046	0.029	0.033	0.025	0.028	0.027	0.031	0.029	.037

Table 5: Minimum and maximum statistical properties sea level at tide gauge locations for members of the initial condition ensemble.

	NIS		NMS		NSB		SIS		SMS		SSB	
	Min.	Max.										
Correlation	0.82	0.88	0.79	0.90	0.68	0.82	0.70	0.78	0.07	0.45	0.71	0.82
RMSE	0.081	0.118	0.064	0.086	0.068	0.084	0.082	0.085	0.079	0.088	0.040	0.069

Table 6: Minimum and maximum statistical properties of principal axis velocities at the mooring locations for members of the initial condition ensemble.

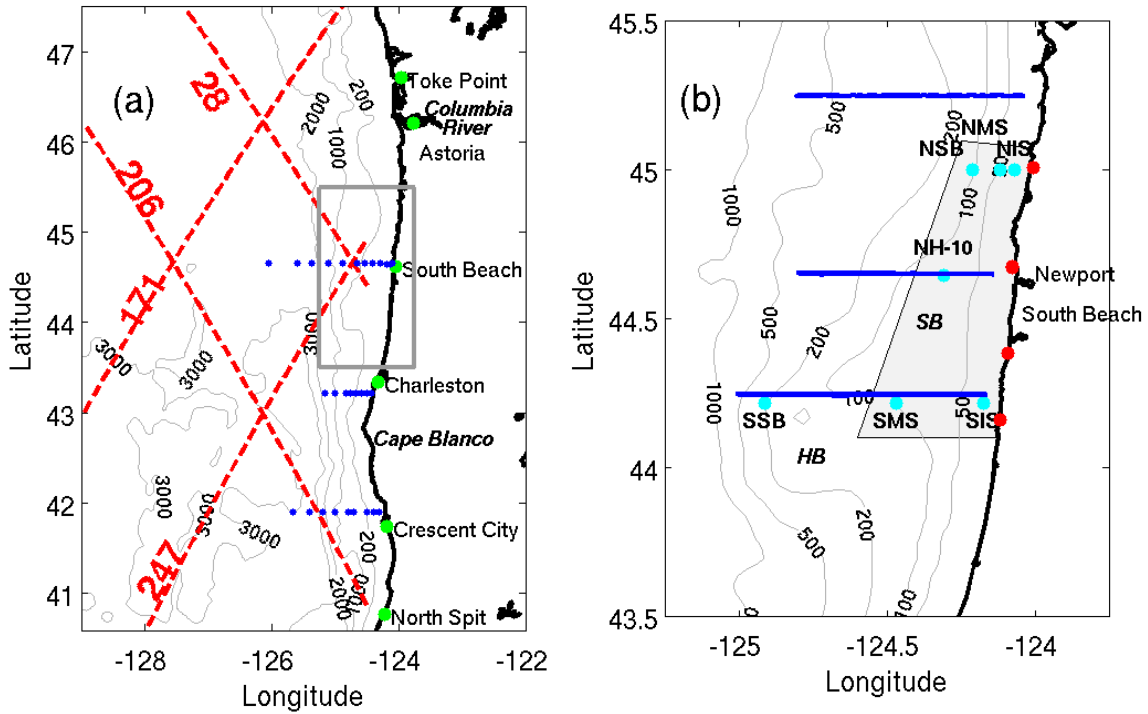


Figure 1: (a) shows the entire model domain with contours of the smoothed bottom topography in meters used in the model. Green dots along the coast show the positions of tide gauges together with their names. The blue dots show the locations of the hydrographic sections used. Dashed red lines are the ground tracks of the TOPEX/Poseidon satellite with their identifiers. (b) A close up of the area enclosed by the gray box in (a) showing details in the vicinity of Heceta Bank (indicated by HB) and Stonewall Bank (SB). Moorings are indicated by light blue dots. The blue lines are the portions of the high-resolution hydrographic survey used here. Red dots are the positions of the HF radar stations, which measure surface currents over the approximate region in the shaded area.

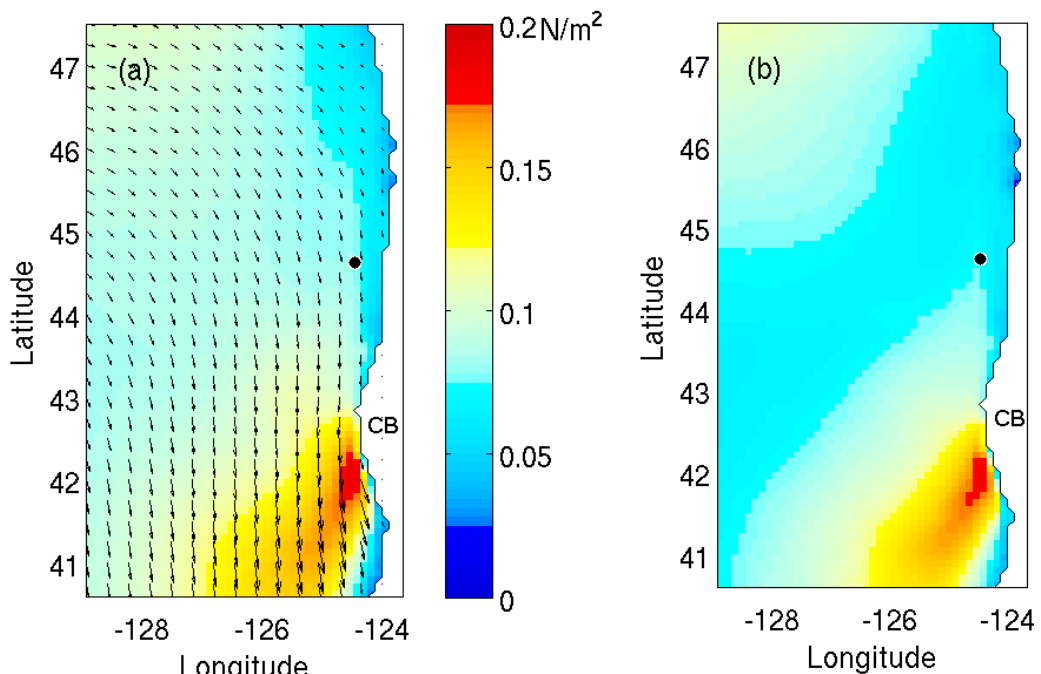


Figure 2: a) Mean and b) standard deviation of wind stress over days 121-305. Vectors show mean wind stress. Black dot indicates position of NOAA buoy 46050. Cape Blanco is designated CB.

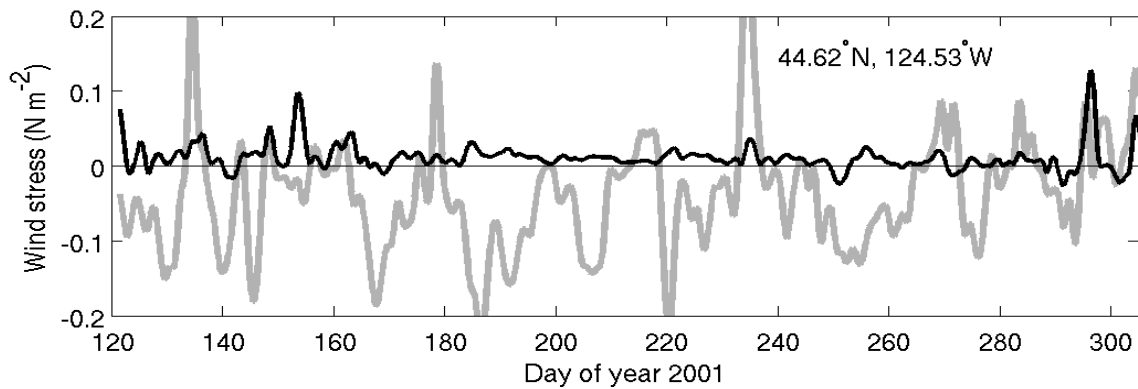


Figure 3: Time series of zonal wind stress (black) and meridional wind stress (gray) sampled from COAMPS model at location closest to NOAA buoy 46050. Prolonged periods of southward, upwelling-favorable winds were interrupted by brief periods of northward, downwelling-favorable winds, or relaxation events.

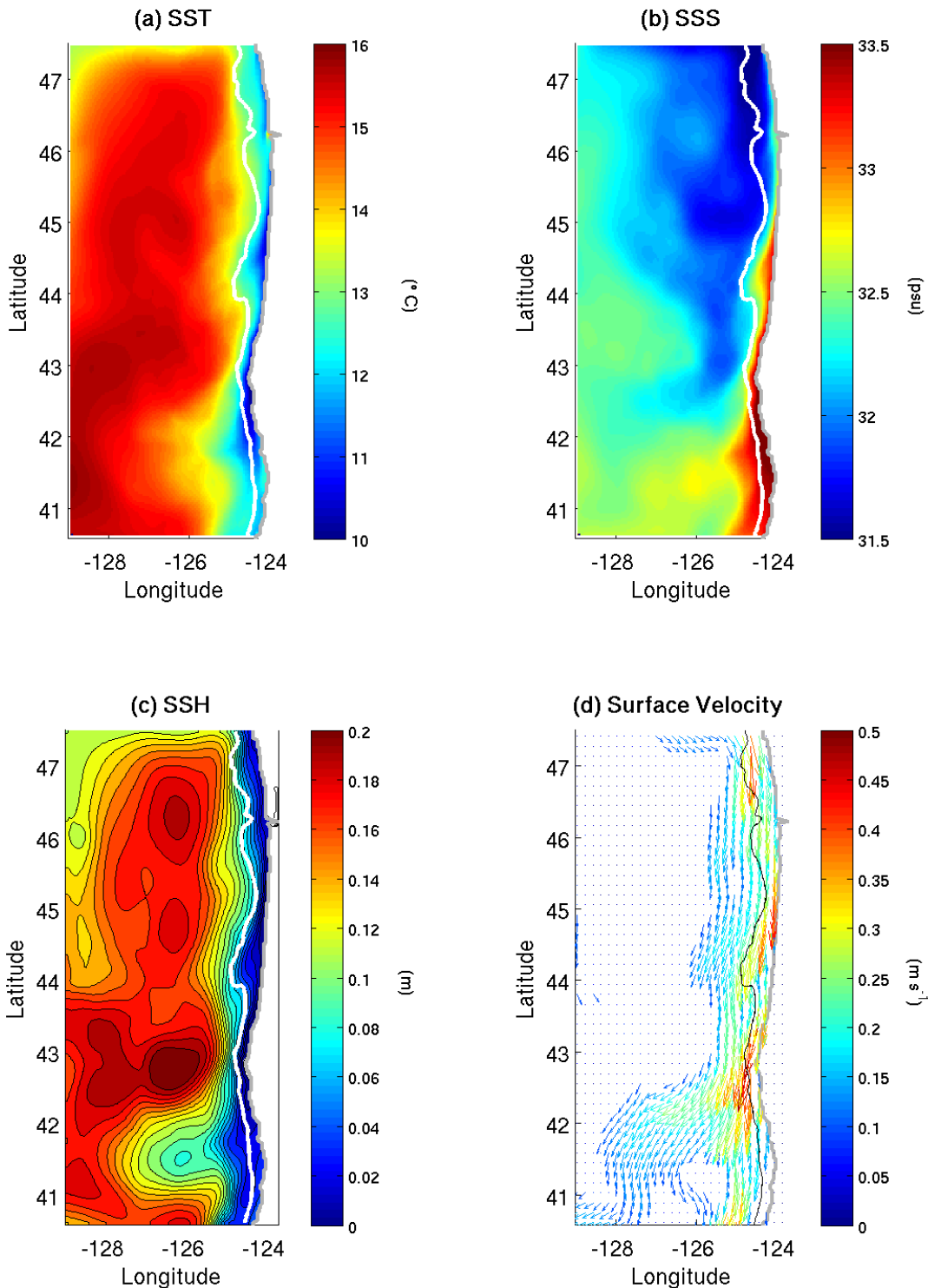


Figure 4: Temporal means (days 121-305) of (a) sea surface temperature ($^{\circ}\text{C}$) (b) sea surface salinity (psu) (c) sea surface height (m) (d) surface velocity vectors colored by speed (ms^{-1}). Vectors are plotted at every fifth grid point and only where the speed is greater than 0.10 ms^{-1} for clarity.

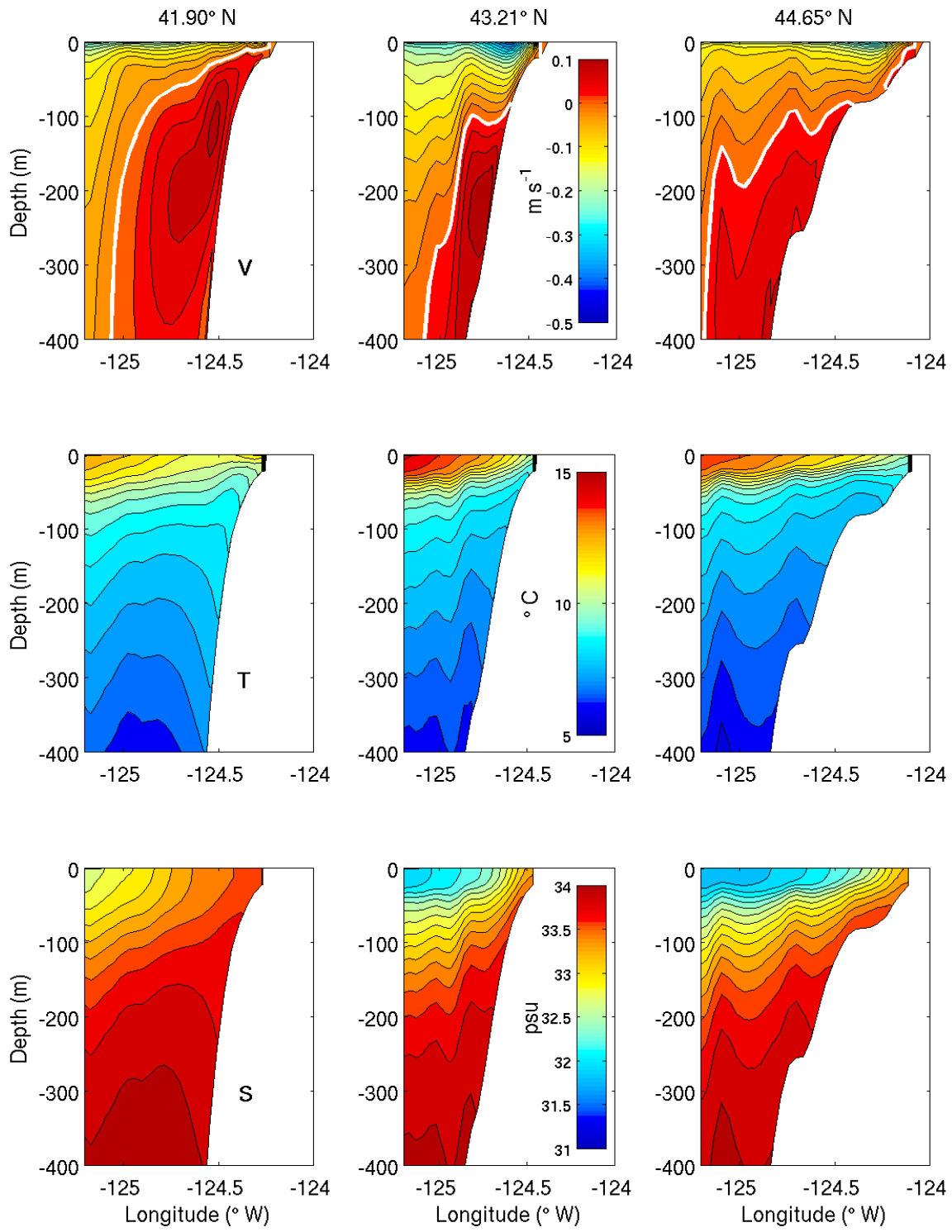


Figure 5: Time mean (days 121-305) of the alongshore velocity ($m s^{-1}$), temperature ($^{\circ}C$), and salinity (psu) on three zonal sections at Crescent City ($41.9^{\circ}N$), Coos Bay ($43.21^{\circ}N$), and Newport ($44.65^{\circ}N$) shown on Figure 1a. The zero contour is indicated by a white contour in the velocity plot.

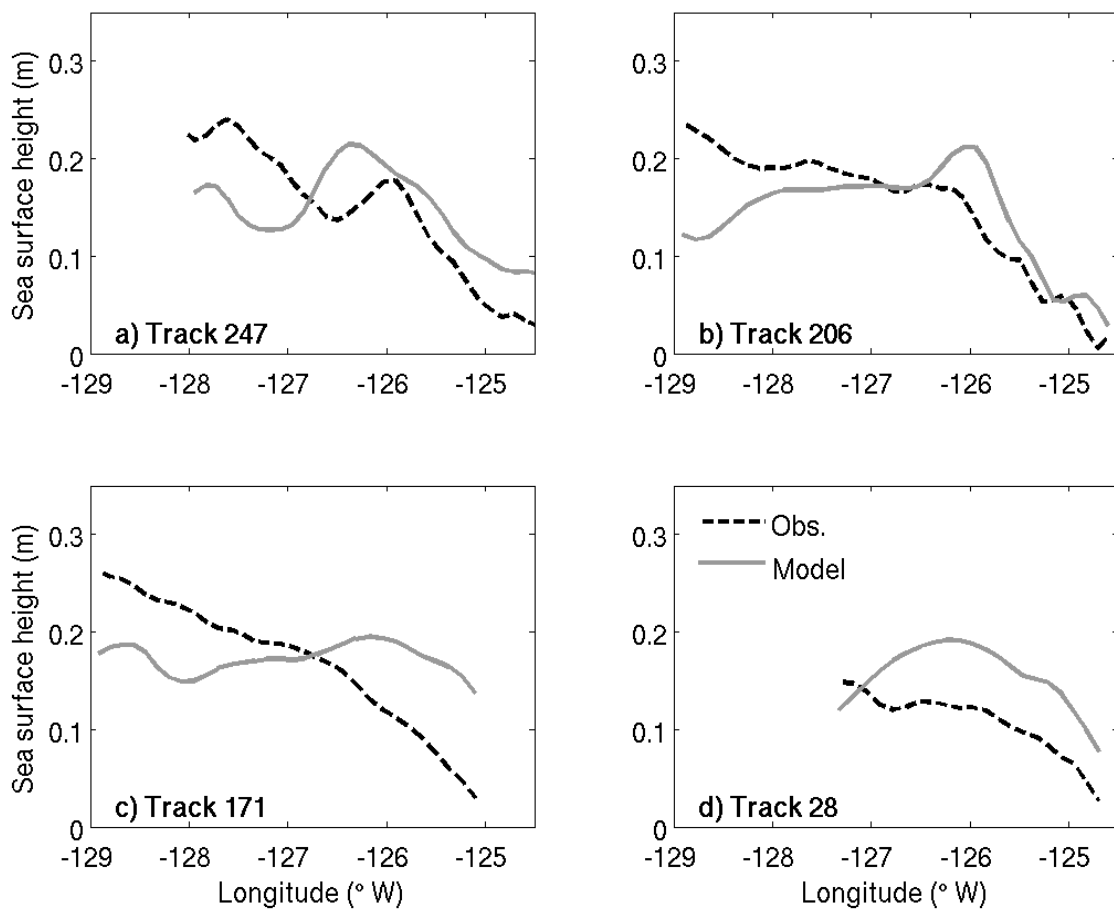


Figure 6: Time averages (days 121-305) of sea surface height along TOPEX/Poseidon tracks. Dashed lines show values from the absolute dynamic topography and solid gray lines show model-simulated values. The abscissa is labeled by longitude, but all of these tracks also cross a range of latitudes due to the inclination of the orbital tracks.

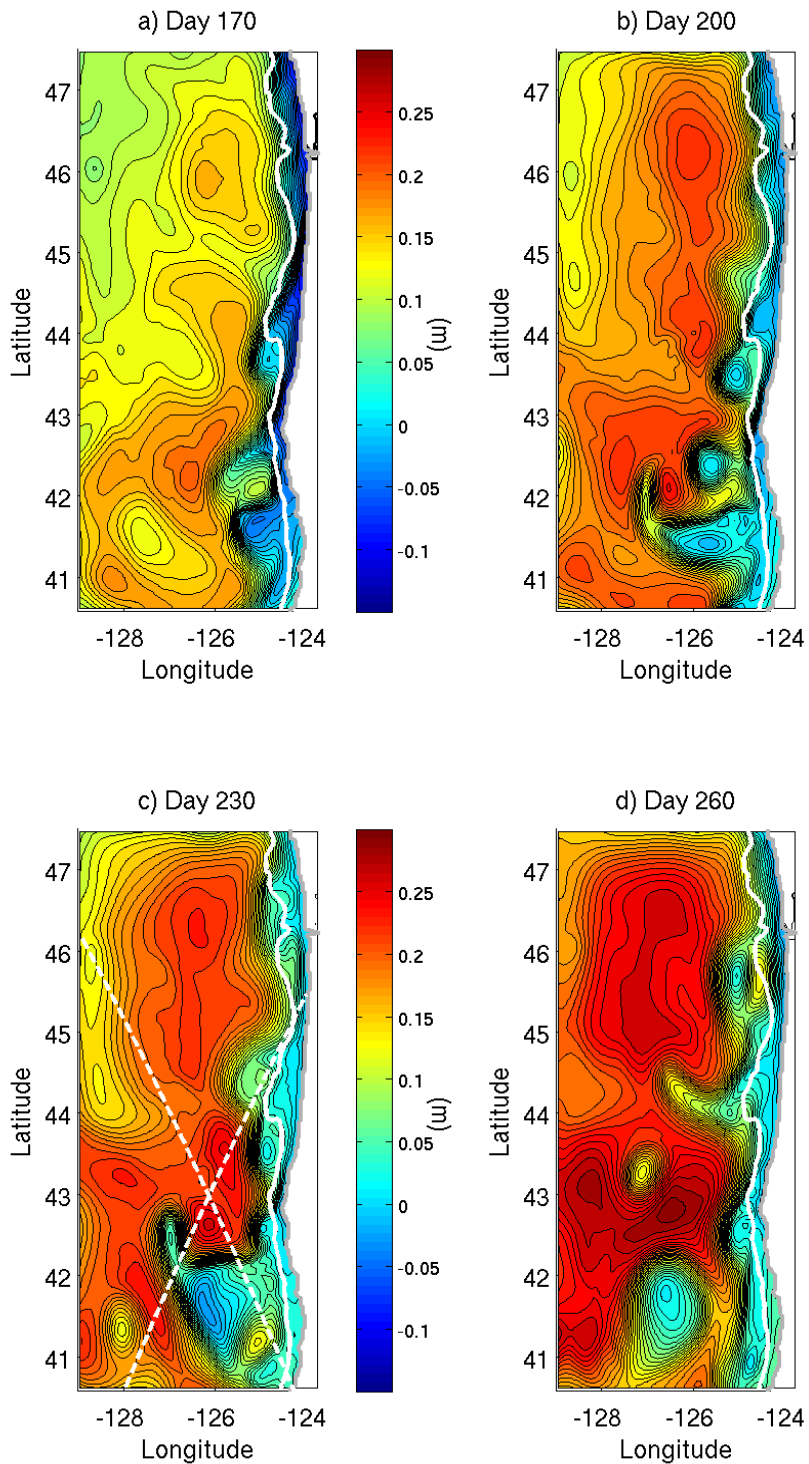


Figure 7: Model-simulated sea surface height on days 170, 200, 230, and 260. A solid white line indicates the 200 m isobath. The intersecting white dashed lines show TOPEX/Poseidon satellite tracks 206 and 247 (Figure 1a).

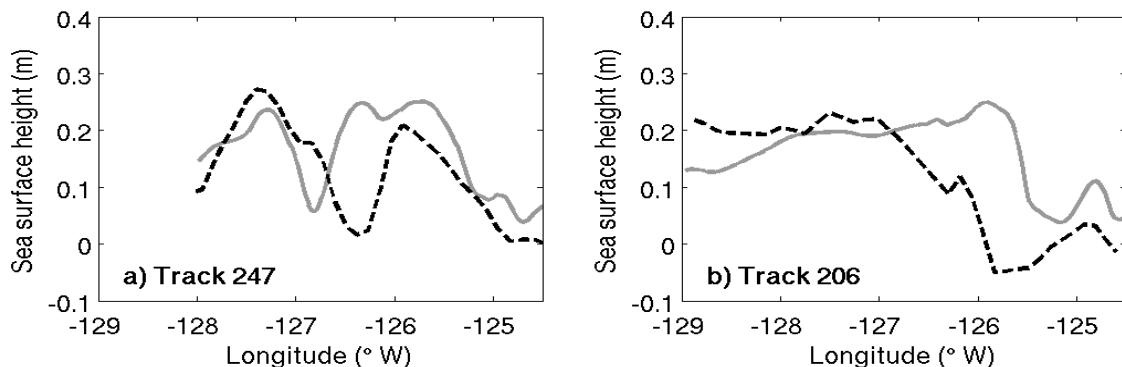


Figure 8: Sea surface height on day 230 estimated from satellite measurements (dashed black line) and model simulation (gray line) on tracks 247 (a) and 206 (b).

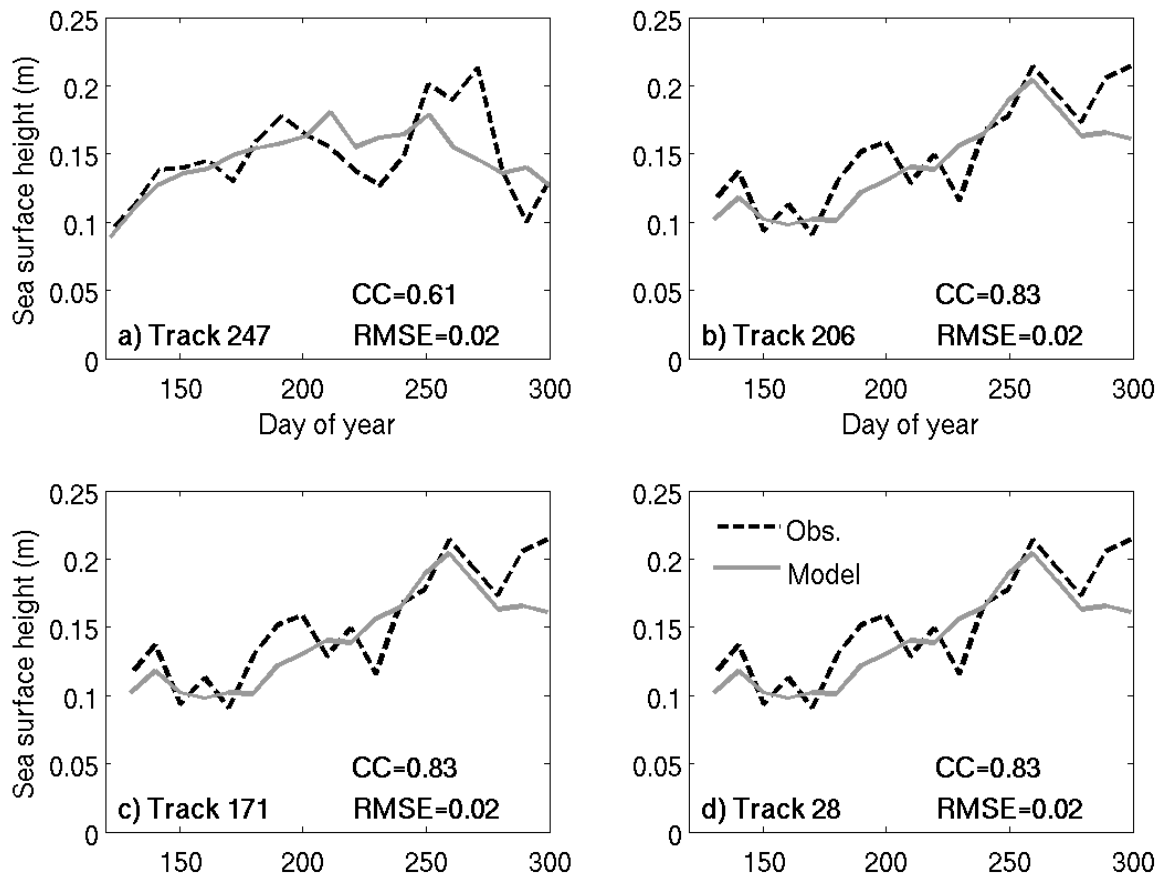


Figure 9: Temporal evolution of sea surface height averaged along TOPEX tracks. The track number is indicated and CC is the correlation coefficient and RMSE is root mean square error. Dashed line is calculated from observations and solid line is calculated from the model simulation.

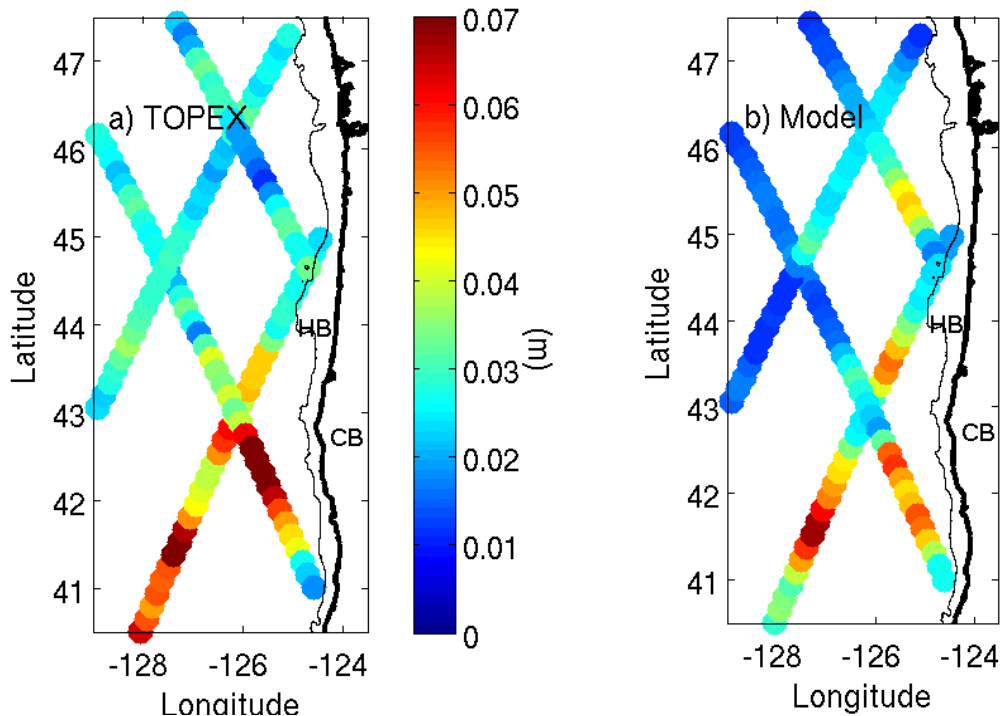


Figure 10: Standard deviation of detrended sea surface height along (a) TOPEX tracks and (b) the model sampled along the tracks. The coastline and the 200 m isobath are also shown. HB is Heceta Bank and CB is Cape Blanco.

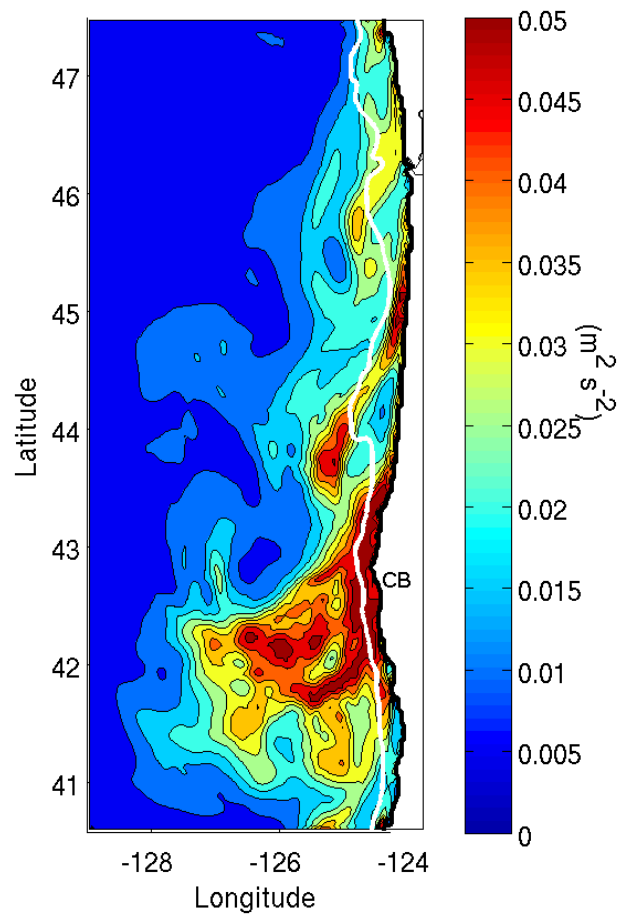


Figure 11: Surface eddy kinetic energy over the interval from day 121 to day 305. The 200 m isobath is indicated with the solid white line and Cape Blanco is marked with CB.

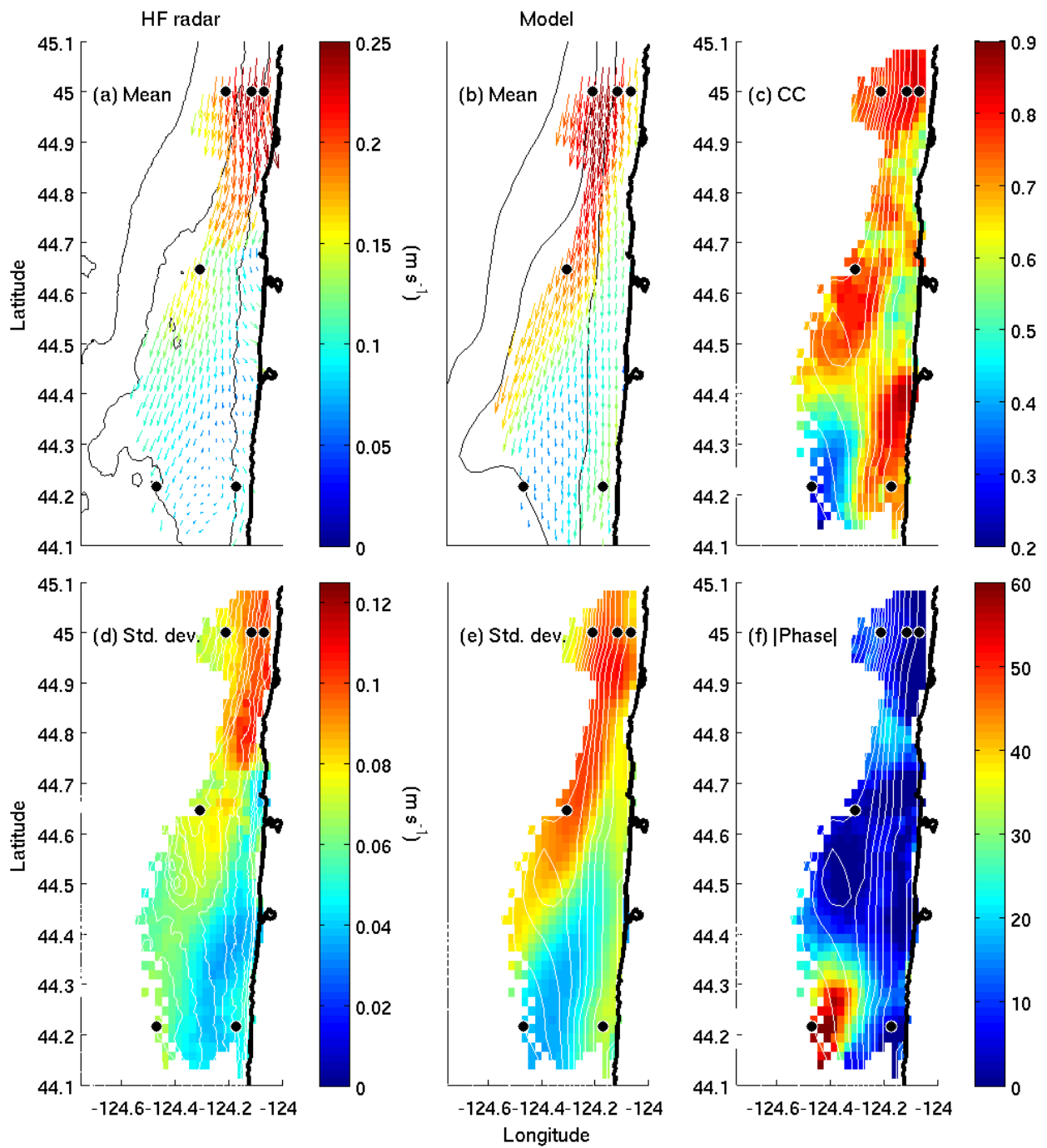


Figure 12: Statistics (days 121-240) for the HF radar array observed [Kosro 2005] and model simulated surface velocities. Mean surface speeds and velocity vectors from observations (a) and model (b). Standard deviation of observations (d) and model. (e) Amplitude of complex correlation [Kundu and Allen, 1976] between observation and model (c) and corresponding phase angle magnitude (degrees) (f). Bottom depth contours are shown. Black dots indicate positions of moorings (see Figure 1b).

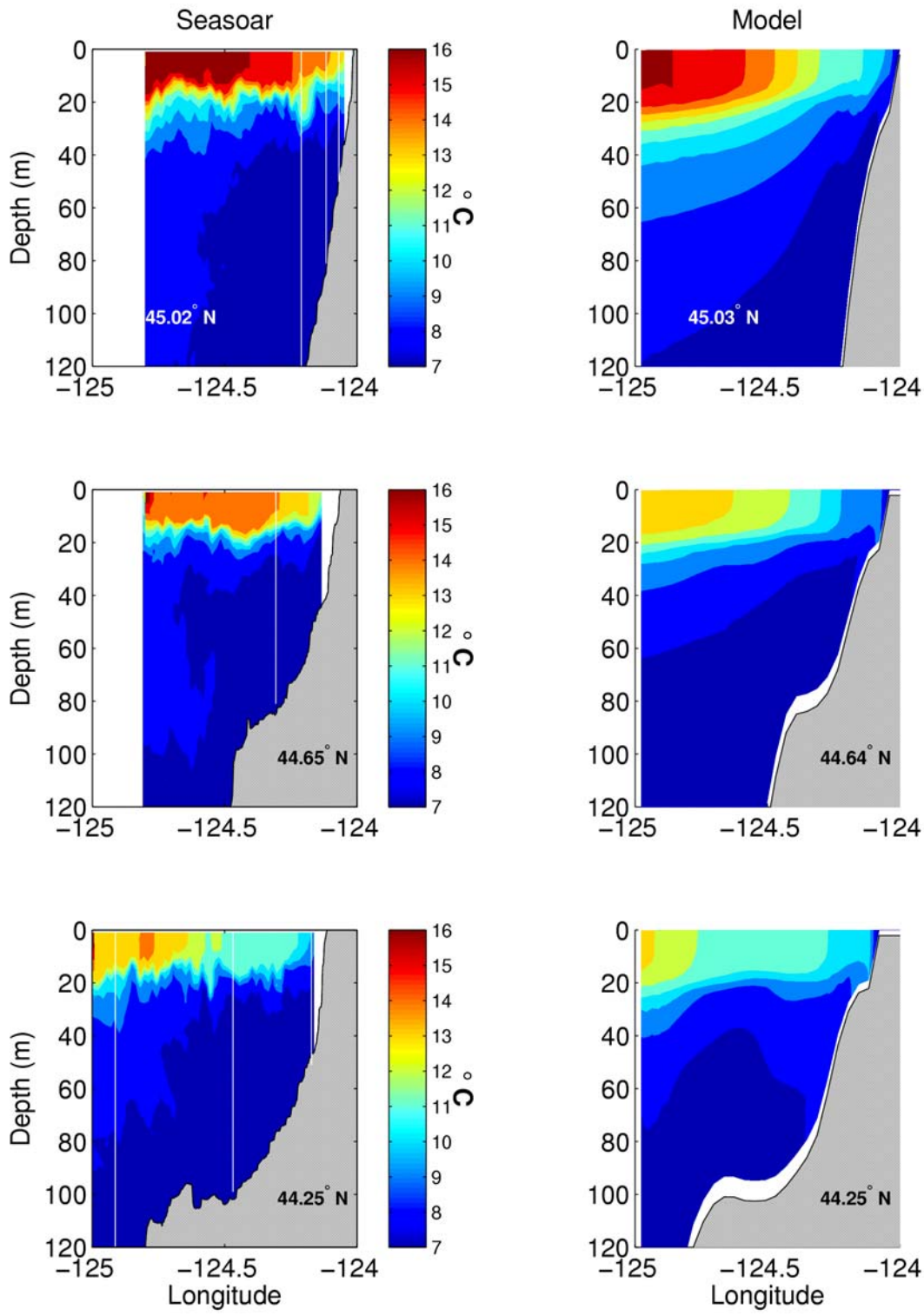


Figure 13: Across-

shore potential temperature sections from hydrographic survey on days 219.3-220.8 (left [Barth et al. 2005]) and model simulation (right) at 45.25° N, 44.65° N, and 44.25° N on day 220.4. The vertical white lines indicate the positions of the moorings.

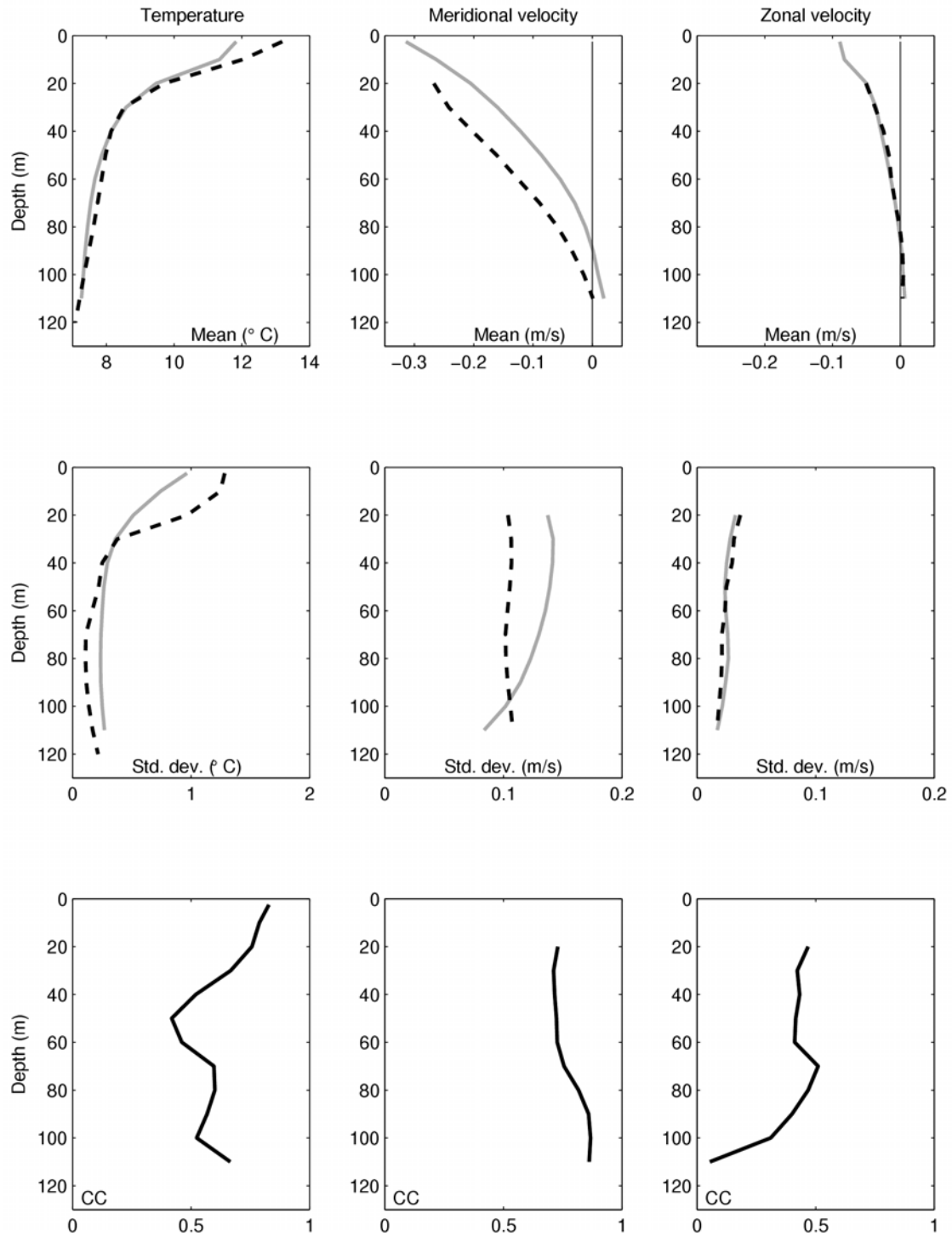


Figure 14: Depth profiles of the statistical properties of T , v , and u at NSB. The dashed line is the observed value [Boyd et al. 2002] and the solid gray line is the model-simulated value. CC indicates cross correlation coefficient.

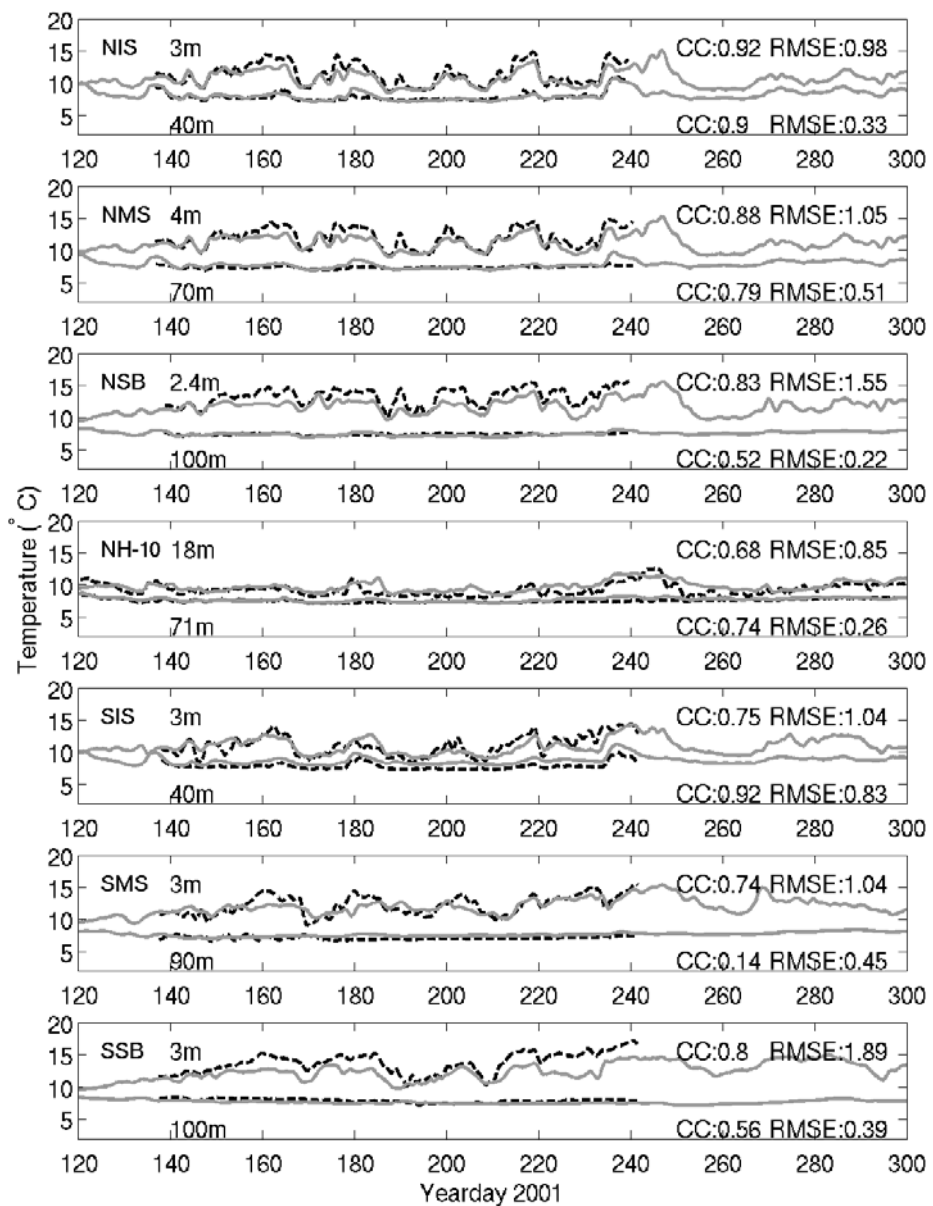


Figure 15: Near-surface and near-bottom temperatures measured at the COAST moorings (dashed line [Boyd et al. 2002]) and simulated in the model (solid gray line). Cross correlation coefficients (CC) and root mean square error (RMSE in m/s) between corresponding observed and modeled temperatures are calculated over the time interval in which there are data.

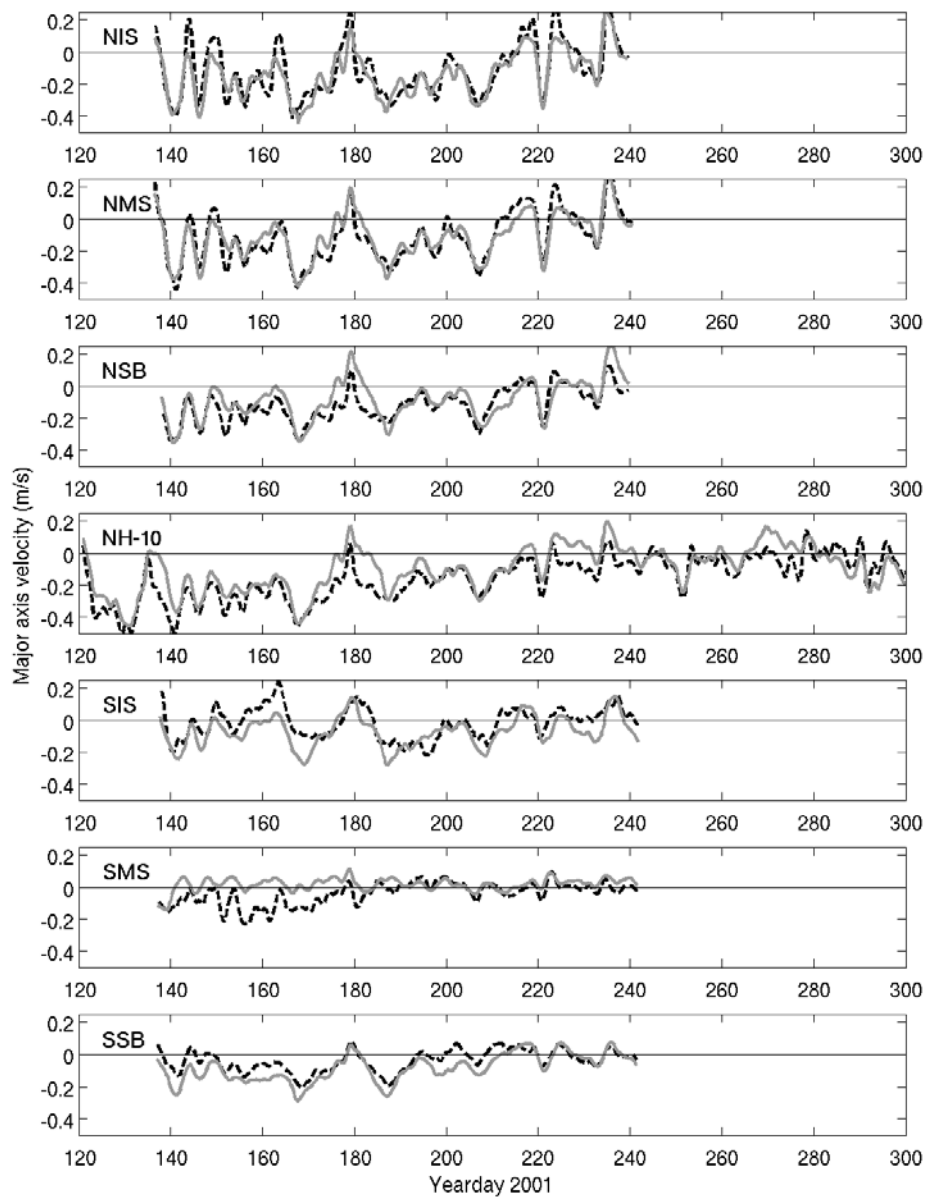


Figure 16: Observed (dashed lines [Boyd et al. 2002]) and model simulated (solid line) vertically averaged velocities in the direction of the major axis of variability. Statistics of the time series are presented in Table 1.

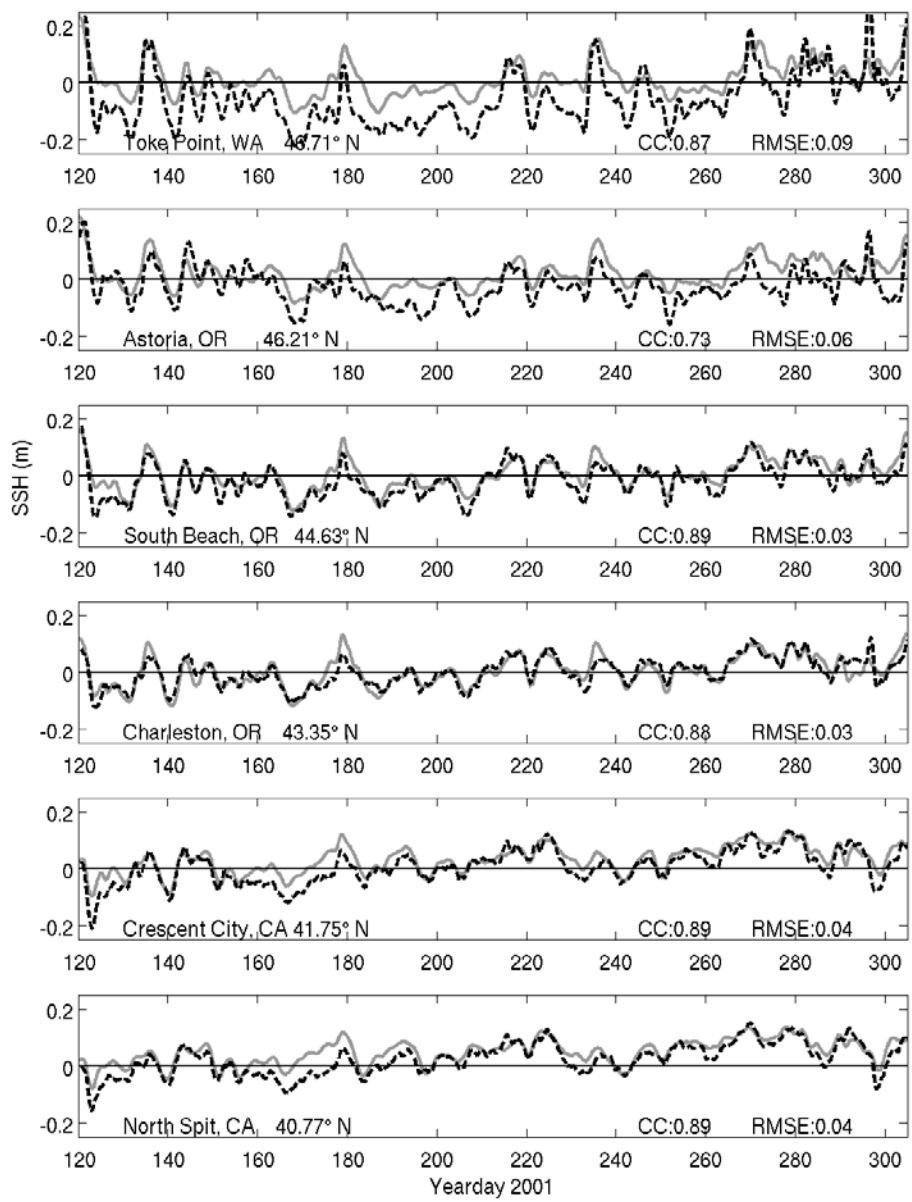


Figure 17: Low pass filtered sea level (with annual mean for 2001 removed) measured at tide gauges (dashed black) and sampled (without removing mean) from model simulation (solid gray). CC is cross correlation coefficient and RMSE is root mean square error. Time period is entire duration of the model simulation.

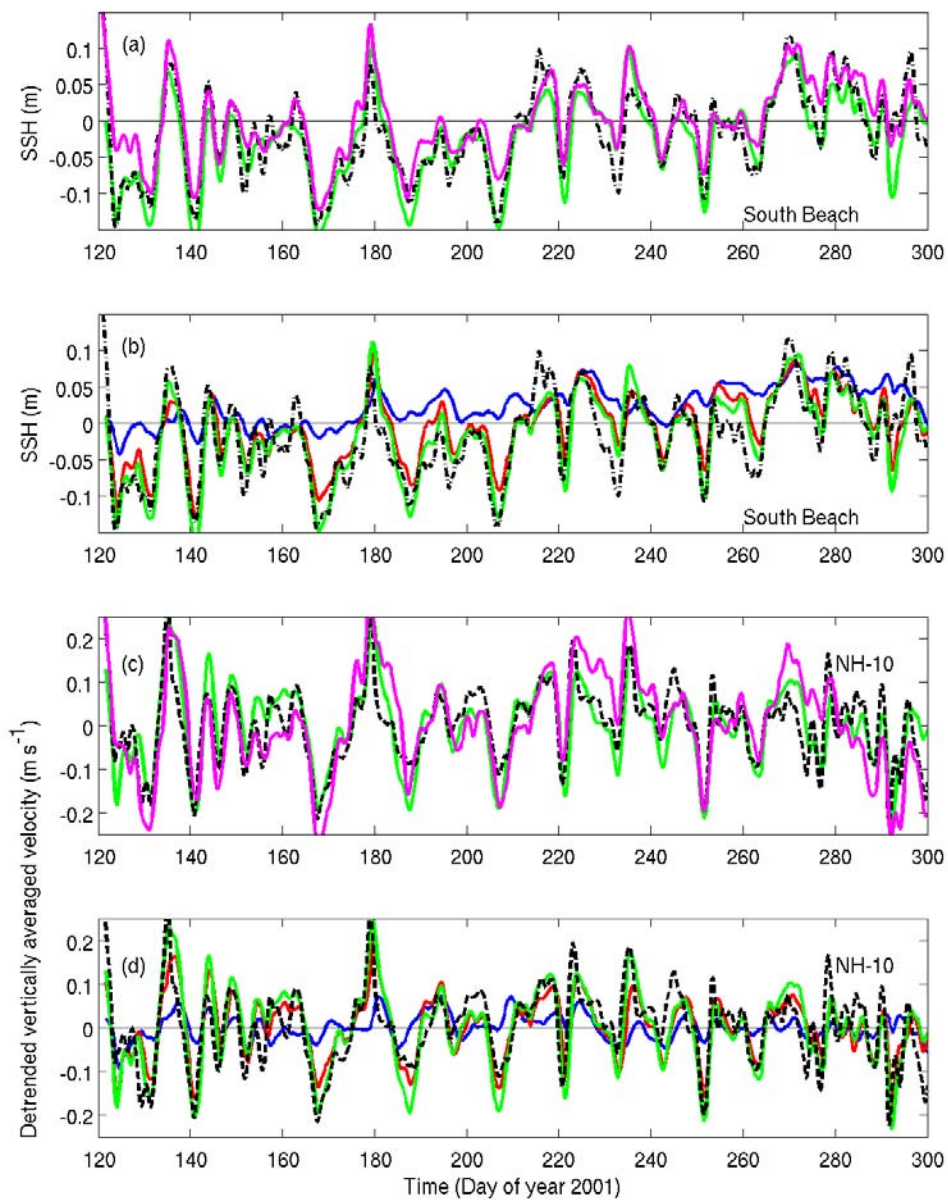


Figure 18:(a) Coastal sea level at South Beach, Oregon, as measured by tide gauge (black dashed), and as modeled by ROMS (magenta) and by one-dimensional wave equation (green). (b) Contributions of wave forcing along wave characteristic at the tide gauge. Blue:southern boundary condition, Red: addition of wind forcing between 40.5° N and 42.75° N, Green: addition of wind forcing between 42.75° N and 45° N) (c) Detrended, vertically averaged velocity at NH-10 as measured (black dashed), modeled by ROMS (magenta), and modeled by wave equation (green). (d) as in (b), but for velocities at NH-10..

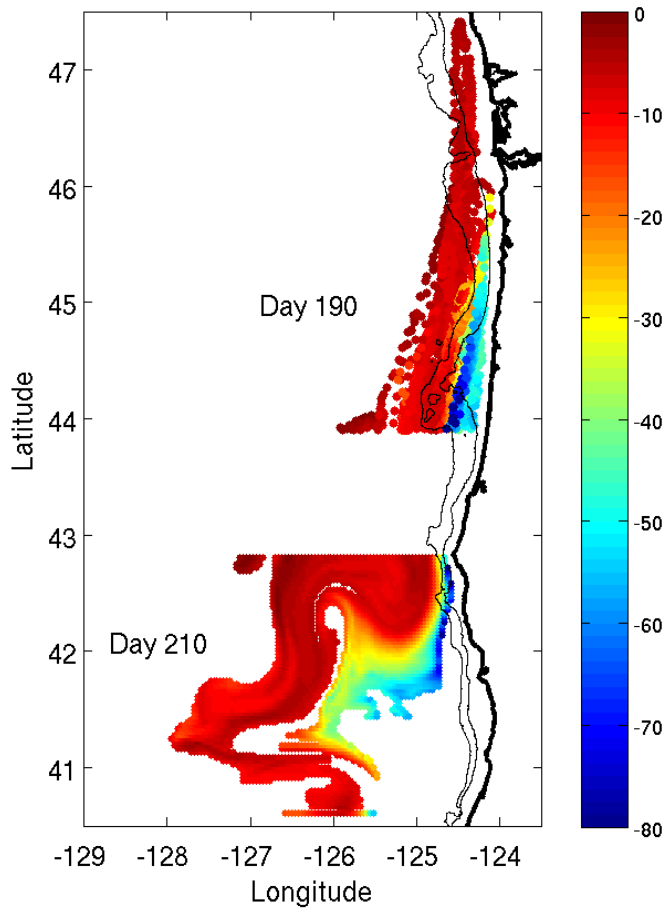


Figure 19: Lagrangian label tracer location on day 190 (north of 44° N) and the same patch of tracer at the surface on day 210 (south of 42.8° N). At both times color corresponds to the depth of the tracer on day 190. The white spaces between the dots on day 190 arise because the inverse mapping to initial positions does not preserve continuity. The white spaces on day 210 indicate regions where the water at the surface did not originate north of 44° N within the given time frame.

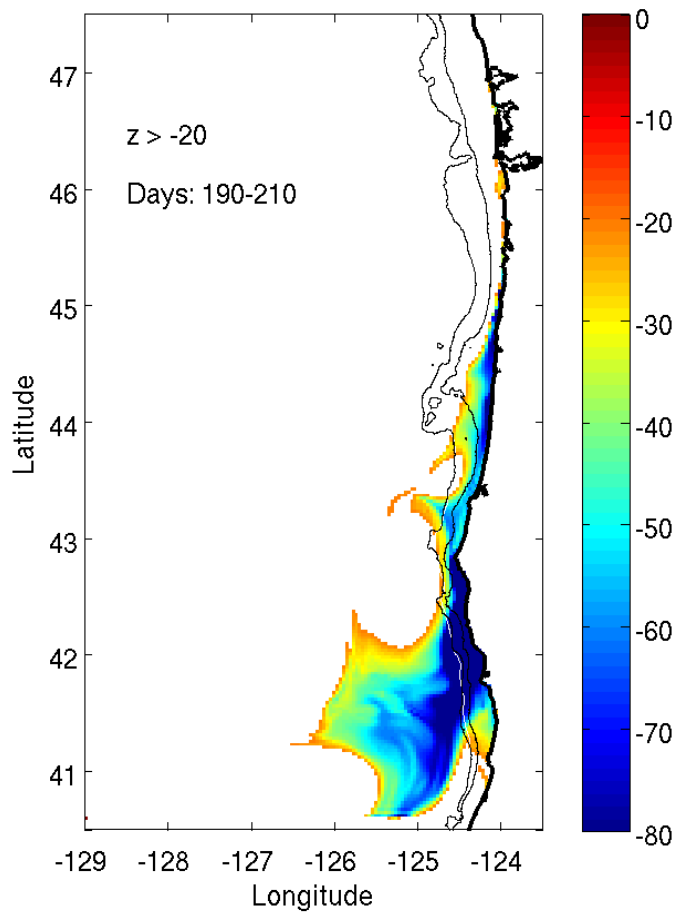


Figure 20: All Lagrangian labels that were deeper than 20 m on day 190 but are at the surface on day 210. Compared with Figure 19, the additional area of upwelled water in the south is due to upwelling that occurred south of Cape Blanco rather than around Heceta Bank

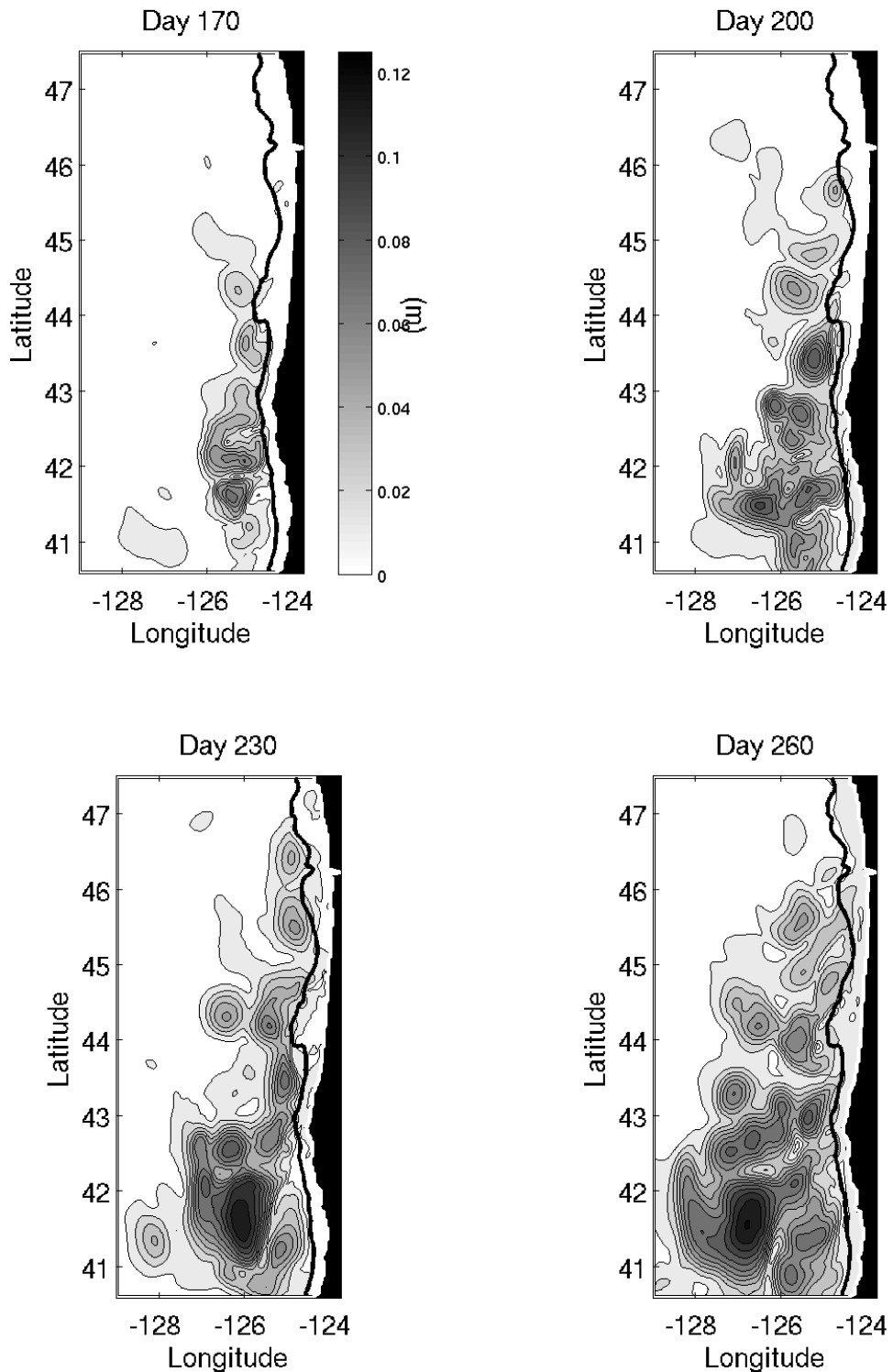


Figure 21.: Ensemble standard deviation of sea surface height for model runs initialized on different days. The solid black line shows the 200 m isobath.

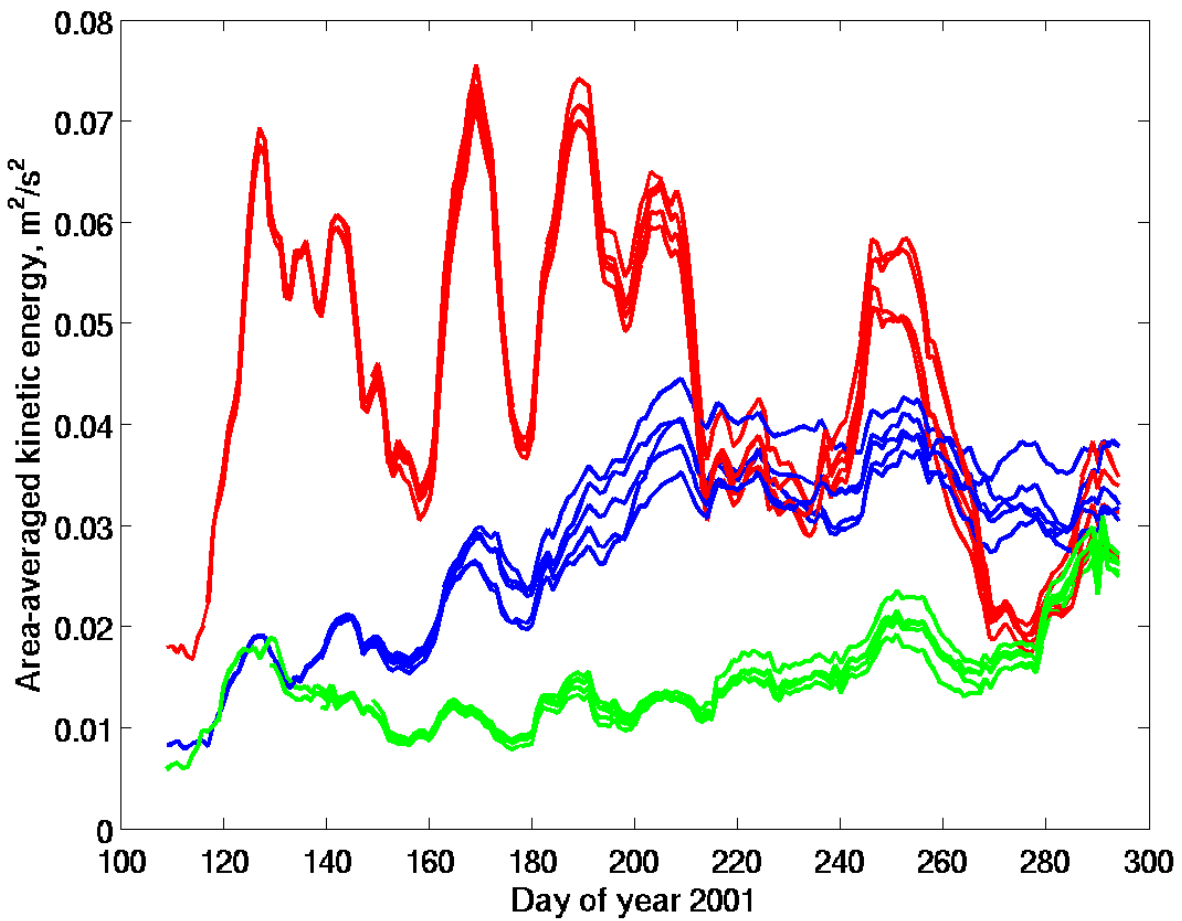


Figure 22: Area-averaged surface kinetic energy within three subdomains: red is coastal subdomain, green is northern offshore subdomain, and blue is southern offshore subdomain (see text for definitions of subdomains). Associated with each subdomain are five lines corresponding to the different members of the ensemble.